A&A 660, A2 (2022)
https://doi.org/10.1051/0004-6361/202142778

Astronomy & Astrophysics

The discovery of a radio galaxy of at least 5 Mpc

Martijn S. S. L. Oei[1], Reinout J. van Weeren[1], Martin J. Hardcastle[2], Andrea Botteon[1], Tim W. Shimwell[1], Pratik Dabhade[3], Aivin R. D. J. G. I. B. Gast[4], Huub J. A. Röttgering[1], Marcus Brüggen[5], Cyril Tasse[6,7], Wendy L. Williams[1], and Aleksandar Shulevski[1]

[1] Leiden Observatory, Leiden University, Niels Bohrweg 2, 2300 RA Leiden, The Netherlands
e-mail: oei@strw.leidenuniv.nl
[2] Centre for Astrophysics Research, University of Hertfordshire, College Lane, Hatfield AL10 9AB, UK
[3] Observatoire de Paris, LERMA, Collège de France, CNRS, PSL University, Sorbonne University, 75014 Paris, France
[4] Somerville College, University of Oxford, Woodstock Road, Oxford OX2 6HD, UK
[5] Hamburger Sternwarte, University of Hamburg, Gojenbergsweg 112, 21029 Hamburg, Germany
[6] GEPI & USN, Observatoire de Paris, Université PSL, CNRS, 5 place Jules Janssen, 92190 Meudon, France
[7] Department of Physics & Electronics, Rhodes University, PO Box 94, Grahamstown 6140, South Africa

Received 29 November 2021 / Accepted 7 February 2022

ABSTRACT

Context. Giant radio galaxies (GRGs, or colloquially 'giants') are the Universe's largest structures generated by individual galaxies. They comprise synchrotron-radiating active galactic nucleus ejecta and attain cosmological (megaparsec-scale) lengths. However, the main mechanisms that drive their exceptional growth remain poorly understood.

Aims. To deduce the main mechanisms that drive a phenomenon, it is usually instructive to study extreme examples. If there exist host galaxy characteristics that are an important cause for GRG growth, then the hosts of the largest GRGs are likely to possess them. Similarly, if there exist particular large-scale environments that are highly conducive to GRG growth, then the largest GRGs are likely to reside in them. For these reasons, we aim to perform a case study of the largest GRG available.

Methods. We reprocessed the LOFAR Two-Metre Sky Survey DR2 by subtracting compact sources and performing multi-scale CLEAN de-convolutions at 60″ and 90″ resolution. The resulting images constitute the most sensitive survey yet for radio galaxy lobes, whose diffuse nature and steep synchrotron spectra have allowed them to evade previous detection attempts at higher resolution and shorter wavelengths. We visually searched these images for GRGs.

Results. We have discovered Alcyoneus, a low-excitation radio galaxy with a projected proper length $l_{\rm p} = 4.99 \pm 0.04$ Mpc. Both its jets and lobes are detected at very high significance, and the SDSS-based identification of the host, at spectroscopic redshift $z_{\rm spec} = 0.24674 \pm 6\times10^{-5}$, is unambiguous. The total luminosity density at $\nu = 144$ MHz is $L_\nu = 8\pm1\times10^{25}$ W Hz^{-1}, which is below average, though near median (percentile 45±3%) for GRGs. The host is an elliptical galaxy with a stellar mass $M_\star = 2.4\pm0.4\times10^{11}\ M_\odot$ and a super-massive black hole mass $M_\bullet = 4 \pm 2 \times 10^8\ M_\odot$, both of which tend towards the lower end of their respective GRG distributions (percentiles 25 ± 9% and 23 ± 11%). The host resides in a filament of the Cosmic Web. Through a new Bayesian model for radio galaxy lobes in three dimensions, we estimate the pressures in the megaparsec-cubed-scale northern and southern lobes to be $P_{\rm min,1} = 4.8 \pm 0.3 \times 10^{-16}$ Pa and $P_{\rm min,2} = 4.9 \pm 0.6 \times 10^{-16}$ Pa, respectively. The corresponding magnetic field strengths are $B_{\rm min,1} = 46 \pm 1$ pT and $B_{\rm min,2} = 46 \pm 3$ pT.

Conclusions. We have discovered what is in projection the largest known structure made by a single galaxy – a GRG with a projected proper length $l_{\rm p} = 4.99 \pm 0.04$ Mpc. The true proper length is at least $l_{\rm min} = 5.04 \pm 0.05$ Mpc. Beyond geometry, Alcyoneus and its host are suspiciously ordinary: the total low-frequency luminosity density, stellar mass, and super-massive black hole mass are all lower than, though similar to, those of the medial GRG. Thus, very massive galaxies or central black holes are not necessary to grow large giants, and, if the observed state is representative of the source over its lifetime, neither is high radio power. A low-density environment remains a possible explanation. The source resides in a filament of the Cosmic Web, with which it might have significant thermodynamic interaction. The pressures in the lobes are the lowest hitherto found, and Alcyoneus therefore represents the most promising radio galaxy yet to probe the warm–hot inter-galactic medium.

Key words. galaxies: active – galaxies: individual: Alcyoneus – galaxies: jets – intergalactic medium – radio continuum: galaxies

1. Introduction

Most galactic bulges hold a super-massive ($M_\bullet > 10^6\ M_\odot$) Kerr black hole (e.g. Soltan 1982) that grows by accreting gas, dust, and stars from its surroundings (Kormendy & Ho 2013). The black hole ejects a fraction of its accretion disk plasma from the host galaxy along two collimated, magnetised jets that are aligned with its rotation axis (e.g. Blandford & Rees 1974). The relativistic electrons contained herein experience Lorentz force and generate, through spiral motion, synchrotron radiation that is observed by radio telescopes. The two jets either fade gradually or end in hotspots at the end of diffuse lobes and ultimately enrich the inter-galactic medium with cosmic rays and magnetic fields. The full luminous structure is referred to as a 'radio galaxy' (RG). Members of a rare RG sub-population attain megaparsec-scale proper (and thus also co-moving) lengths (e.g. Willis et al. 1974; Andernach et al. 1992; Ishwara-Chandra & Saikia 1999; Jamrozy et al. 2008; Machalski 2011; Kuźmicz et al. 2018; Dabhade et al. 2020a). The definition of giant radio galaxies (GRGs, or colloquially 'giants') accommodates our

limited ability to infer an RG's true proper length from observations: an RG is called a GRG if and only if its proper length projected onto the plane of the sky exceeds some threshold, $l_{\rm p,GRG}$, usually chosen to be 0.7 or 1 Mpc. Because the conversion between angular length and projected proper length depends on cosmological parameters, which remain uncertain, it is not always clear whether a given observed RG satisfies the GRG definition.

Currently, there are about a thousand GRGs known, the majority of which have been found in the northern sky. About one hundred exceed 2 Mpc, and ten exceed 3 Mpc; at 4.9 Mpc, the literature's projectively longest GRG is J1420-0545 (Machalski et al. 2008). As such, GRGs – and the rest of the megaparsec-scale RGs – are the largest single-galaxy–induced phenomena in the Universe. Which physical mechanisms lead some RGs to extend for $\sim 10^2$ times their host galaxy diameter is a key open question. To determine whether there exist particular host galaxy characteristics or large-scale environments that are essential for GRG growth, it is instructive to analyse the largest GRGs, since in these systems it is most likely that all major favourable growth factors are present. We thus aim to perform a case study of the largest GRG available.

As demonstrated by Dabhade et al. (2020b)'s record sample of 225 discoveries, the Low-Frequency Array (LOFAR; van Haarlem et al. 2013) is among the most attractive contemporary instruments for finding new GRGs. This pan-European radio interferometer features a unique combination of short baselines to provide sensitivity to large-scale emission and long baselines to mitigate source confusion[1]. These qualities are indispensable for observational studies of GRGs, which require both extended lobes and compact cores and jets to be identified. Additionally, the metre wavelengths at which the LOFAR operates allow it to detect steep-spectrum lobes far away from host galaxies. Such lobes reveal the full extent of GRGs but are missed by decimetre observatories.

Thus, in Sect. 2 we describe a reprocessing of the LOFAR Two-Metre Sky Survey (LoTSS) Data Release 2 (DR2) aimed at revealing hitherto unknown RG lobes – among other goals. An overview of the reprocessed images, which cover thousands of square degrees, and statistics of the lengths and environments of the GRGs they have revealed are subjects of future publications. In the present article we introduce Alcyoneus[2], a 5 Mpc GRG that these images allowed us to discover. We determine and discuss its properties in Sect. 3. Figure 1 provides a multi-wavelength, multi-resolution view of this giant. Section 4 contains our concluding remarks.

We assume a concordance Λ cold dark matter cosmology with parameters $\mathfrak{M}$ from Planck Collaboration VI (2020): $\mathfrak{M} = (h = 0.6766, \Omega_{\rm BM,0} = 0.0490, \Omega_{\rm M,0} = 0.3111, \Omega_{\Lambda,0} = 0.6889)$, where $H_0 := h \cdot 100$ km s^{-1} Mpc^{-1}. We define the spectral index α such that it relates to flux density F_ν at frequency ν as $F_\nu \propto \nu^\alpha$. Regarding terminology, we strictly distinguish between an RG (a radio-bright structure of relativistic particles and magnetic fields, consisting of a core, jets, hotspots, and lobes) and the host galaxy that generates it.

2. Data and methods

The LoTSS, conducted by the LOFAR High-Band Antennae (HBA), is a 120–168 MHz interferometric survey (Shimwell et al. 2017, 2019, 2022) with the ultimate aim to image the full northern sky at resolutions of 6″, 20″, 60″, and 90″. Its central frequency $\nu_{\rm c} = 144$ MHz. The latest data release – the LoTSS DR2 (Shimwell et al. 2022) – covers 27% of the northern sky, split over two regions of 4178 deg^2 and 1457 deg^2; the largest of these contains the Sloan Digital Sky Survey (SDSS) DR7 (Abazajian et al. 2009) area. By default, the LoTSS DR2 provides imagery at the 6″ and 20″ resolutions. We show these standard products in Fig. 2 for the same sky region as in Fig. 1. In terms of total source counts, the LoTSS DR2 is the largest radio survey carried out thus far: its catalogue contains 4.4×10^6 sources, most of which are considered 'compact'.

By contrast, the 60″ and 90″ imagery, which we discuss in more detail in Oei et al. (in prep.), is intended to reveal extended structures in the low-frequency radio sky, such as GRGs, supernova remnants in the Milky Way, radio halos and shocks in galaxy clusters, and – potentially – accretion shocks or volume-filling emission from filaments of the Cosmic Web. To avoid the source confusion limit at these resolutions, following van Weeren et al. (2021), we used DDFacet (Tasse et al. 2018) to predict visibilities corresponding to the 20″ LoTSS DR2 sky model and subtracted these from the data, before imaging at 60″ and 90″ with WSClean IDG (Offringa et al. 2014; van der Tol et al. 2018). We used −0.5 Briggs weighting and multi-scale CLEAN (Offringa & Smirnov 2017), with `-multiscale-scales 0,4,8,16,32,64`. Importantly, we did not impose an inner (u, v)-cut. We imaged each pointing separately, then combined the partially overlapping images into a mosaic by calculating, for each direction, a beam-weighted average.

Finally, we visually searched the LoTSS DR2 for GRGs, primarily at 6″ and 60″, using the Hierarchical Progressive Survey (HiPS) system in *Aladin Desktop 11.0* (Bonnarel et al. 2000).

3. Results and discussion

3.1. Radio morphology and interpretation

During our LoTSS DR2 search, we identified a three-component radio structure of total angular length $\phi = 20.8'$, visible at all (6″, 20″, 60″ and 90″) resolutions. Figure 2 provides a sense of our data quality; it shows that the outer components are barely discernible in the LoTSS DR2 at its standard 6″ and 20″ resolutions. Meanwhile, Fig. 1 shows the outer components at 60″, and the top panel of Fig. 9 shows them at 90″; at these resolutions, they lie firmly above the noise. Compared with the outer structures, the central structure is bright and elongated, with a 155″ major axis and a 20″ minor axis. The outer structures lie along the major axis at similar distances from the central structure, are diffuse and amorphous, and feature specific intensity maxima along this axis.

In the arcminute-scale vicinity of the outer structures, the DESI Legacy Imaging Surveys (Dey et al. 2019) DR9 does not reveal galaxy overdensities or low-redshift spiral galaxies, the ROSAT All-Sky Survey (RASS; Voges et al. 1999) does not show X-ray brightness above the noise, and there is no *Planck* Sunyaev–Zeldovich Catalogue 2 (PSZ2; Planck Collaboration XXVII 2016) source nearby. The outer structures therefore

[1] Source confusion is an instrumental limitation that arises when the resolution of an image is low compared to the sky density of statistically significant sources. It causes angularly adjacent but physically unrelated sources to blend together, making it hard or even impossible to distinguish them (e.g. Condon et al. 2012).

[2] Alcyoneus was the son of Ouranos, the Greek primordial god of the sky. According to Ps.-Apollodorus, he was also one of the greatest of the Gigantes (Giants) and a challenger to Heracles during the Gigantomachy – the battle between the Giants and the Olympian gods for supremacy over the cosmos. The poet Pindar described him as 'huge as a mountain', fighting by hurling rocks at his foes.

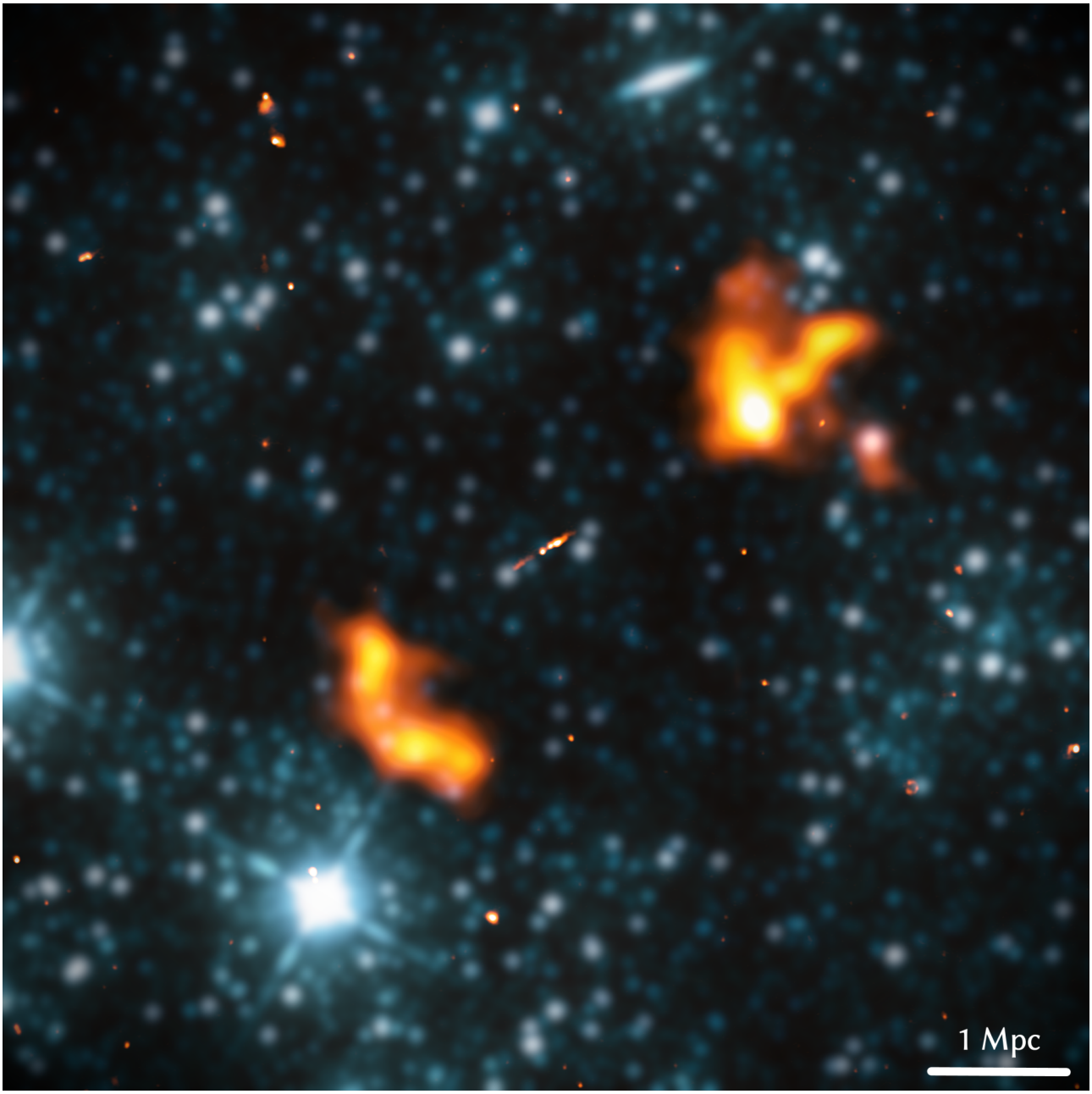

Fig. 1. Joint radio-infrared view of Alcyoneus, a radio galaxy with a projected proper length of 5.0 Mpc. We show a 2048″ × 2048″ solid angle centred around right ascension 123.590372° and declination 52.402795°. We superimpose LoTSS DR2 images at 144 MHz of two different resolutions (6″ for the core and jets, and 60″ for the lobes) (orange), with the WISE image at 3.4 µm (blue). To highlight the radio emission, the infrared emission has been blurred to 0.5′ resolution.

cannot be supernova remnants in low-redshift spiral galaxies or radio relics and radio halos in galaxy clusters. Instead, the outer structures presumably represent RG emission.

The radio-optical overlays in the top and bottom panels of Fig. 3 show that it is improbable that each outer structure is an RG of its own, given the lack of significant 6″ radio emission (solid light green contours) around host galaxy candidates suggested by the morphology of the 60″ radio emission (translucent white contours). For these reasons, we interpret the central (jet-like) structure and the outer (lobe-like) structures as components of the same RG.

Subsequent analysis – presented below – demonstrates that this RG is the largest hitherto discovered, with a projected proper length of 5.0 Mpc. We dub this GRG 'Alcyoneus'.

3.2. Host galaxy identification

Based on the middle panel of Fig. 3 and an SDSS DR12 (Alam et al. 2015) spectrum, we identify a source at a J2000 right ascension of 123.590372°, a declination of 52.402795° and a spectroscopic redshift of $z_{\rm spec} = 0.24674 \pm 6 \times 10^{-5}$ as Alcyoneus's host. Like most GRG hosts, this source, with SDSS DR12 name J081421.68+522410.0, is an elliptical galaxy[3] without a quasar. From optical contours, we find that the galaxy's minor axis makes a ~20° angle with Alcyoneus's jet axis.

In Fig. 4 we further explore the connection between J081421.68+522410.0 and Alcyoneus's radio core and jets.

[3] Based on the SDSS morphology, Kuminski & Shamir (2016) calculate a probability of 89% that the galaxy is an elliptical.

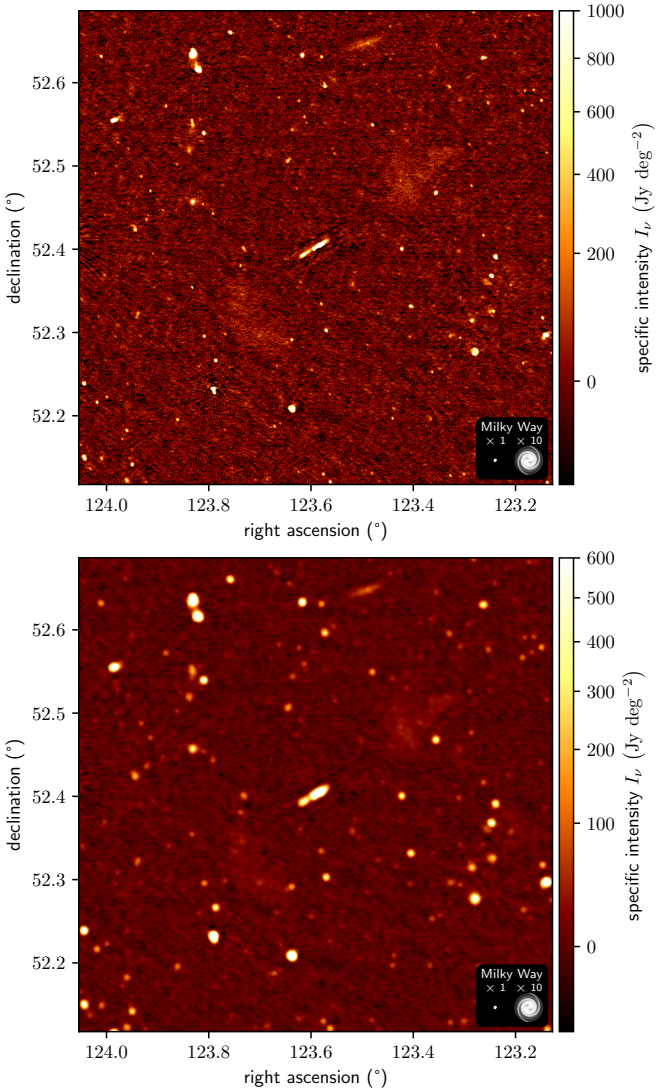

Fig. 2. LoTSS DR2 images of Alcyoneus, centred around host galaxy J081421.68+522410.0, at central frequency $\nu_c = 144$ MHz and standard resolutions $\theta_{FWHM} = 6''$ (*top*) and $\theta_{FWHM} = 20''$ (*bottom*). At these resolutions, Alcyoneus's lobes are easily overlooked. For scale, we show the stellar Milky Way disk (diameter: 50 kpc) and a ten-times-inflated version; the spiral galaxy shape follows Ringermacher & Mead (2009).

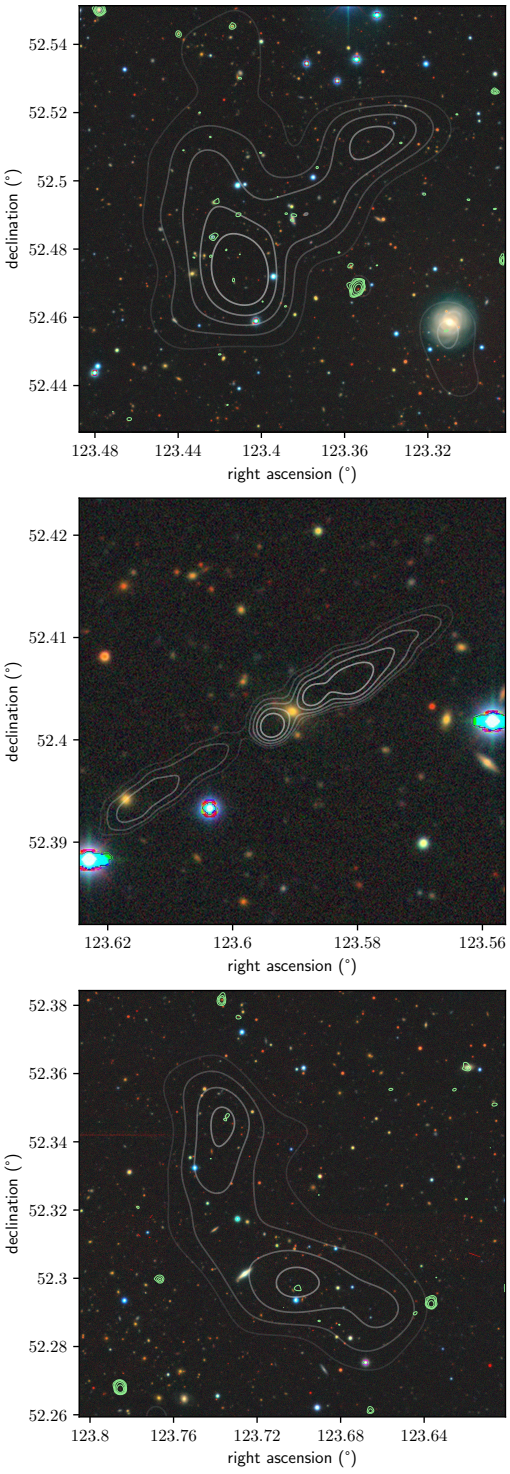

Fig. 3. Joint radio-optical views showing that the outer structures shown in Fig. 1 are best interpreted as a pair of RG lobes fed by central jets. On top of DESI Legacy Imaging Surveys DR9 (g, r, z) imagery, we show the LoTSS DR2 at various resolutions through contours at multiples of σ, where σ is the image noise at the relevant resolution. *Top and bottom panels*: translucent white $60''$ contours at $3, 5, 7, 9, 11\sigma$ and solid light green $6''$ contours at $4, 7, 10, 20, 40\sigma$. *Central panel*: translucent white $6''$ contours at $5, 10, 20, 40, 80\sigma$.

From top to bottom, we show the LoTSS DR2 at $6''$, the Very Large Array Sky Survey (VLASS; Lacy et al. 2020) at $2.2''$, and the Panoramic Survey Telescope and Rapid Response System (Pan-STARRS) DR1 (Chambers et al. 2016) i band. Two facts confirm that the host identification is highly certain. First, for both the LoTSS DR2 at $6''$ and the VLASS at $2.2''$, the angular separation between J081421.68+522410.0 and the arc connecting Alcyoneus's two innermost jet features is at the subarcsecond scale. Moreover, the alleged host galaxy is the brightest Pan-STARRS DR1 i-band source within a radius of $45''$ of the central VLASS image component.

3.3. Radiative- or jet-mode active galactic nucleus

Current understanding (e.g. Heckman & Best 2014) suggests that the population of active galactic nuclei (AGN) exhibits a dichotomy: AGN seem to be either radiative-mode AGN, which generate high-excitation radio galaxies (HERGs), or jet-mode AGN, which generate low-excitation radio galaxies (LERGs). We wished to determine if Alcyoneus is a HERG or a LERG. The SDSS spectrum of the host features very weak emission lines;

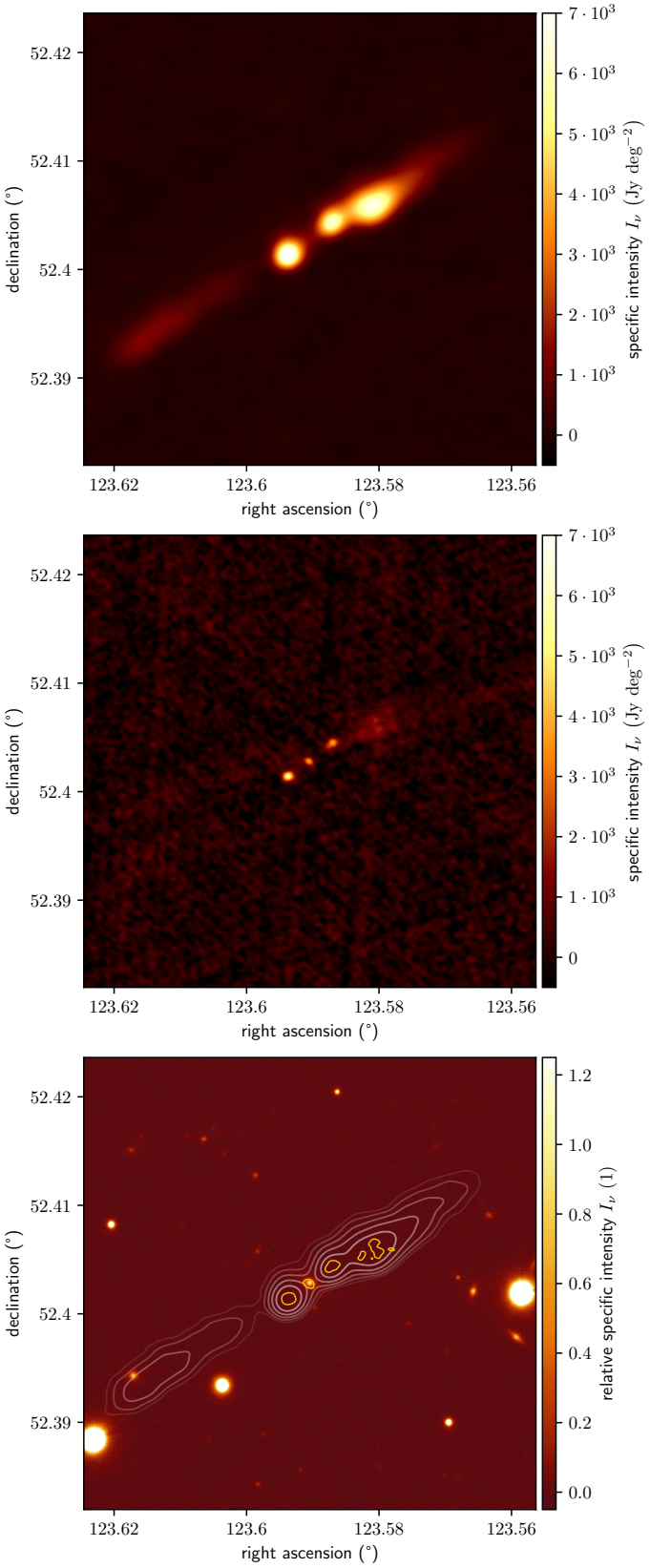

Fig. 4. Radio and optical specific intensity function details around the SDSS DR12 source J081421.68+522410.0, Alcyoneus's host galaxy. The panels cover a 2.5′×2.5′ region around the host, an elliptical galaxy with spectroscopic redshift $z_{\rm spec} = 0.24674 \pm 6 \times 10^{-5}$. *From top to bottom*: we show the LoTSS DR2 6″, the VLASS 2.2″, and the Pan-STARRS DR1 *i* band relative to the host's specific intensity with LoTSS contours (white) as in Fig. 3 and a VLASS contour (gold) at 5σ.

indeed, the star formation rate is just $1.6 \times 10^{-2}\ M_\odot\ {\rm yr}^{-1}$ (Chang et al. 2015). Following the classification rule of Best & Heckman (2012), Best et al. (2014), Pracy et al. (2016), and Williams et al. (2018) based on the strength and equivalent width of the OIII 5007 Å line, we determined that Alcyoneus is a LERG. Moreover, the Wide-Field Infrared Survey Explorer (WISE) photometry (Cutri et al. 2012) at 11.6 µm and 22.1 µm is below the instrumental detection limit. Following the classification rule of Gürkan et al. (2014) based on the 22.1 µm luminosity density, we affirmed that Alcyoneus is a LERG. Through automated classification, Best & Heckman (2012) came to the same conclusion.

Being a jet-mode AGN, the super-massive black hole (SMBH) in the centre of Alcyoneus's host galaxy presumably accretes at an efficiency below 1% of the Eddington limit and is fuelled mainly by slowly cooling hot gas.

3.4. Projected proper length

We calculated Alcyoneus's projected proper length $l_{\rm p}$ through its angular length ϕ and spectroscopic redshift $z_{\rm spec}$. We formally determined $\phi = 20.8'' \pm 0.15''$ from the compact-source–subtracted 90″ image (top panel of Fig. 9) by selecting the largest great-circle distance between all possible pairs of pixels with a specific intensity higher than three sigma-clipped standard deviations above the sigma-clipped median. We find $l_{\rm p} = 4.99 \pm 0.04$ Mpc; this makes Alcyoneus the projectively largest RG known.

Methodology details and a probabilistic comparison between the projected proper lengths of Alcyoneus and J1420-0545 are given in Appendix A.

3.5. Radio luminosity densities and kinetic jet powers

From the LoTSS DR2 6″ image (top panel of Fig. 4), we measured that two northern jet local maxima occur at angular distances of $9.2 \pm 0.2''$ and $23.7 \pm 0.2''$ from the host, or at projected proper distances of 36.8 ± 0.8 kpc and 94.8 ± 0.8 kpc. Two southern jet local maxima occur at angular distances of $8.8 \pm 0.2''$ and $62.5 \pm 0.2''$ from the host, or at projected proper distances of 35.2 ± 0.8 kpc and 249.9 ± 0.8 kpc.

At the central observing frequency of $\nu_{\rm c} = 144$ MHz, the northern jet has a flux density $F_\nu = 193 \pm 20$ mJy, the southern jet has $F_\nu = 110 \pm 12$ mJy, whilst the northern lobe has $F_\nu = 63 \pm 7$ mJy and the southern lobe has $F_\nu = 44 \pm 5$ mJy. To minimise contamination from fore- and background galaxies, we determined the lobe flux densities from the compact-source–subtracted 90″ image. The flux density uncertainties are dominated by the 10% flux scale uncertainty inherent to the LoTSS DR2 (Shimwell et al. 2022). The host galaxy flux density is relatively weak, and the corresponding emission has, at $\nu_{\rm c} = 144$ MHz and 6″ resolution, no clear angular separation from the inner jets' emission; we have therefore not determined it.

Due to cosmological redshifting, the conversion between flux density and luminosity density depends on the spectral indices α of Alcyoneus's luminous components. We estimated the spectral indices of the core and jets from the LoTSS DR2 6″ and VLASS 2.2″ images. After convolving the VLASS image with a Gaussian to the common resolution of 6″, we calculated the mean spectral index between the LoTSS central frequency $\nu_{\rm c} = 144$ MHz and the VLASS central frequency $\nu_{\rm c} = 2.99$ GHz. Using only directions for which both images have a significance of at least 5σ, we deduced a core spectral index $\alpha = -0.25 \pm 0.1$ and a combined inner jet spectral index $\alpha = -0.65 \pm 0.1$. The

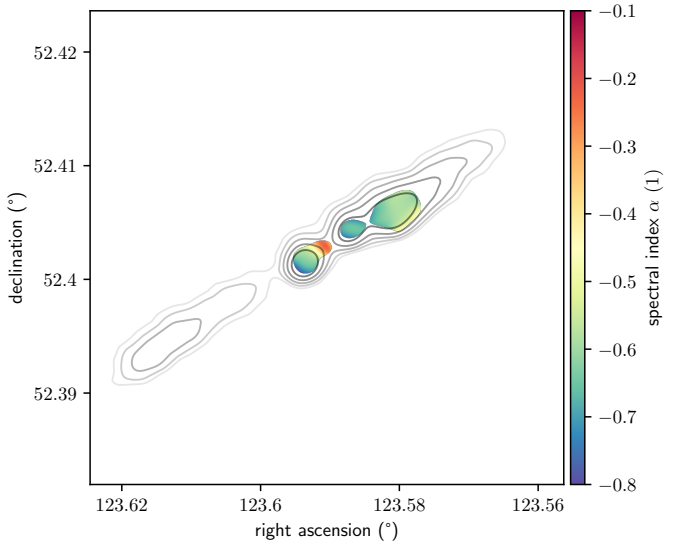

Fig. 5. LoTSS–VLASS spectral index map, revealing Alcyoneus's flat-spectrum core and steeper-spectrum jets. We show all directions where both the LoTSS and VLASS images have at least 5σ significance. In black, we overlay the same LoTSS contours as in Figs. 3 and 4. The core spectral index is $\alpha = -0.25 \pm 0.1$, and the combined inner jet spectral index is $\alpha = -0.65 \pm 0.1$.

Table 1. Luminosity densities L_ν (in 10^{24} W Hz^{-1}) of Alcyoneus's lobes for three potential spectral indices α at rest-frame frequency $\nu = 144$ MHz.

	$\alpha = -0.8$	$\alpha = -1.2$	$\alpha = -1.6$
Northern lobe	12 ± 1	13 ± 1	14 ± 1
Southern lobe	8.3 ± 0.8	9.0 ± 0.9	9.9 ± 1

spectral index uncertainties are dominated by the LoTSS DR2 and VLASS flux scale uncertainties. We show the full spectral index map in Fig. 5.

We have not determined the spectral index of the lobes, as they are only detected in the LoTSS imagery.

The luminosity densities of the northern and southern jet at rest-frame frequency $\nu = 144$ MHz are $L_\nu = (3.6 \pm 0.4) \times 10^{25}$ W Hz^{-1} and $L_\nu = (2.0 \pm 0.2) \times 10^{25}$ W Hz^{-1}, respectively. Following Dabhade et al. (2020a), we estimated the kinetic power of the jets from their luminosity densities and the results of the simulation-based analytical model of Hardcastle (2018). We find $Q_{\rm jet,1} = 1.2 \pm 0.1 \times 10^{36}$ W and $Q_{\rm jet,2} = 6.6 \pm 0.7 \times 10^{35}$ W, so the total kinetic jet power is $Q_{\rm jets} := Q_{\rm jet,1} + Q_{\rm jet,2} = 1.9 \pm 0.2 \times 10^{36}$ W. Interestingly, this total kinetic jet power is lower than the average $Q_{\rm jets} = 3.7 \times 10^{36}$ W, and close to the median $Q_{\rm jets} = 2.2 \times 10^{36}$ W, for low-excitation GRGs in the redshift range $0.18 < z < 0.43$ (Dabhade et al. 2020a).

Because the lobe spectral indices are unknown, we present luminosity densities for several possible values of α in Table 1[4]. (Because of electron ageing, α will decrease further away from the core.)

Assuming $\alpha = -1.2$, Alcyoneus's total luminosity density at $\nu = 144$ MHz is $L_\nu = 7.8 \pm 0.8 \times 10^{25}$ W Hz^{-1}. In Fig. 6 we compare this estimate to other GRGs' total luminosity density at the same frequency, as found by Dabhade et al. (2020b) through the LoTSS DR1 (Shimwell et al. 2019). Interestingly, Alcyoneus is not particularly luminous: it has a low-frequency luminosity density typical for the currently known GRG population (percentile $45 \pm 3\%$).

[4] The inferred luminosity densities have a cosmology dependence; our results are ∼6% higher than for modern high-H_0 cosmologies.

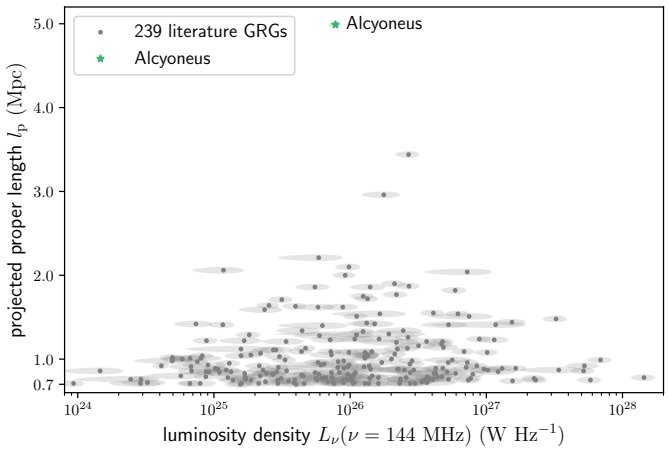

Fig. 6. Relation between the GRG projected proper length $l_{\rm p}$ and total luminosity density L_ν at rest-frame frequency $\nu = 144$ MHz. Total luminosity densities include contributions from all available RG components (i.e. the core, jets, hotspots, and lobes). Literature GRGs are from Dabhade et al. (2020b) and are marked with grey disks, and Alcyoneus is marked with a green star. Translucent ellipses indicate −1 to +1 standard deviation uncertainties. Alcyoneus has a typical luminosity density (percentile $45 \pm 3\%$).

3.6. True proper length from relativistic beaming

Following Hardcastle et al. (1998a), we simultaneously constrained Alcyoneus's jet speed u and inclination angle θ from the jets' flux density asymmetry: the northern-to-southern jet flux density ratio $J = 1.78 \pm 0.3$.[5] We had assumed that the jets propagate with identical speeds in exactly opposite directions (making line-of-sight angles θ and $\theta + 180°$) and have statistically identical relativistic electron populations; as such, they have a common synchrotron spectral index α. Using $\alpha = -0.65 \pm 0.1$ as before and

$$\beta := \frac{u}{c};\ \ \beta\cos\theta = \frac{J^{\frac{1}{2-\alpha}} - 1}{J^{\frac{1}{2-\alpha}} + 1}, \tag{1}$$

we found $\beta\cos\theta = 0.106 \pm 0.03$. Because $\cos\theta \leq 1$, β is bounded from below by $\beta_{\rm min} = 0.106 \pm 0.03$.

From detailed modelling of ten Fanaroff–Riley I RGs (which have jet luminosities comparable to that of Alcyoneus), Laing & Bridle (2014) deduced that initial jet speeds are roughly $\beta = 0.8$, which decrease until roughly $0.6\ r_0$, with r_0 being the recollimation distance. Most of the ten recollimation distances from Laing & Bridle (2014) are between 5 and 15 kpc, with the largest being that of NGC 315: $r_0 = 35$ kpc. Because the local specific intensity maxima in Alcyoneus's jets closest to the host occur at projected proper distances of 36.8 ± 0.8 kpc and 35.2 ± 0.8 kpc, the true proper distances must be even larger. We conclude that the observed jet emission presumably comes from a region farther from the host than r_0, so the initial stage of jet deceleration – in which the jet speed is typically reduced by several tens of

[5] Because J is obtained through the division of two independent normal random variables (RVs) with non-zero mean, J is an RV with an uncorrelated non-central normal ratio distribution.

percents of c – must already be completed. Thus, $\beta_{\rm max} = 0.8$ is a safe upper bound.

Taking $\beta_{\rm max} = 0.8$, θ is bounded from above by $\theta_{\rm max} = 82.4 \pm 2°$ ($\theta \in [0, 90°]$), or bounded from below by $180° - \theta_{\rm max} = 97.6 \pm 2°$ ($\theta \in [90°, 180°]$).[6] If we model Alcyoneus's geometry as a line segment, and assume no jet reorientation, Alcyoneus's true proper length l and projected proper length $l_{\rm p}$ relate as

$$l = \frac{l_{\rm p}}{\sin\theta}; \quad l \geq l_{\rm min} = \frac{l_{\rm p}}{\sin\theta_{\rm max}}. \tag{2}$$

We bounded l from below: $l_{\rm min} = 5.04 \pm 0.05$ Mpc. A triangular prior on β between $\beta_{\rm min}$ and $\beta_{\rm max}$ with the mode at $\beta_{\rm max}$ induces a skewed prior on l; the 90% credible interval is $l \in [5.0\ {\rm Mpc}, 5.5\ {\rm Mpc}]$, with the mean and median being 5.2 Mpc and 5.1 Mpc, respectively. A flat prior on β between $\beta_{\rm min}$ and $\beta_{\rm max}$ also induces a skewed prior on l; the 90% credible interval is $l \in [5.0\ {\rm Mpc}, 7.1\ {\rm Mpc}]$, with the mean and median being 5.6 Mpc and 5.1 Mpc, respectively. The median of l seems particularly well determined, as it is insensitive to variations in the prior on β.

In Appendix B, we explore the inclination angle conditions under which Alcyoneus has the largest true proper length of all known (>4 Mpc) GRGs.

3.7. Stellar mass and super-massive black hole mass

The question then arises as to whether a galaxy or its central black hole needs to be massive in order to generate a GRG. Alcyoneus's host has a stellar mass $M_\star = 2.4 \pm 0.4 \times 10^{11}\ M_\odot$ (Chang et al. 2015). We tested whether or not this is a typical stellar mass among the total known GRG population. We assembled a literature catalogue of 1013 GRGs by merging the compendium of Dabhade et al. (2020a), which is complete up to April 2020, with the GRGs discovered in Galvin et al. (2020), Ishwara-Chandra et al. (2020), Tang et al. (2020), Bassani et al. (2021), Brüggen et al. (2021), Delhaize et al. (2021), Masini et al. (2021), Kuźmicz & Jamrozy (2021), Andernach et al. (2021) and Mahato et al. (2022). We collected stellar masses with uncertainties from Chang et al. (2015), which are based on SDSS and WISE photometry, and from Salim et al. (2018), which are based on Galaxy Evolution Explorer (GALEX), SDSS, and WISE photometry. We gave precedence to the stellar masses by Salim et al. (2018) when both were available. We obtained stellar masses for 151 previously known GRGs. The typical stellar mass range is 10^{11}–$10^{12}\ M_\odot$, the median $M_\star = 3.5 \times 10^{11}\ M_\odot$, and the mean $M_\star = 3.8 \times 10^{11}\ M_\odot$. Strikingly, the top panel of Fig. 7 illustrates that Alcyoneus's host has a fairly low (percentile 25 ± 9%) stellar mass compared with the currently known population of GRG hosts.

For the GRGs in our literature catalogue, we also estimated SMBH masses via the M-sigma relation. We collected SDSS DR12 stellar velocity dispersions with uncertainties (Alam et al. 2015), and applied the M-sigma relation of Eq. (7) in Kormendy & Ho (2013). Alcyoneus's host has a SMBH mass $M_\bullet = 3.9 \pm 1.7 \times 10^8\ M_\odot$. We obtained SMBH masses for 189 previously known GRGs. The typical SMBH mass range is 10^8–$10^{10}\ M_\odot$, the median $M_\bullet = 7.9 \times 10^8\ M_\odot$ and the mean $M_\bullet = 1.5 \times 10^9\ M_\odot$. Strikingly, the bottom panel of Fig. 7 illustrates that Alcyoneus's host has a fairly low (percentile 23±11%) SMBH mass compared with the currently known population of GRG hosts.

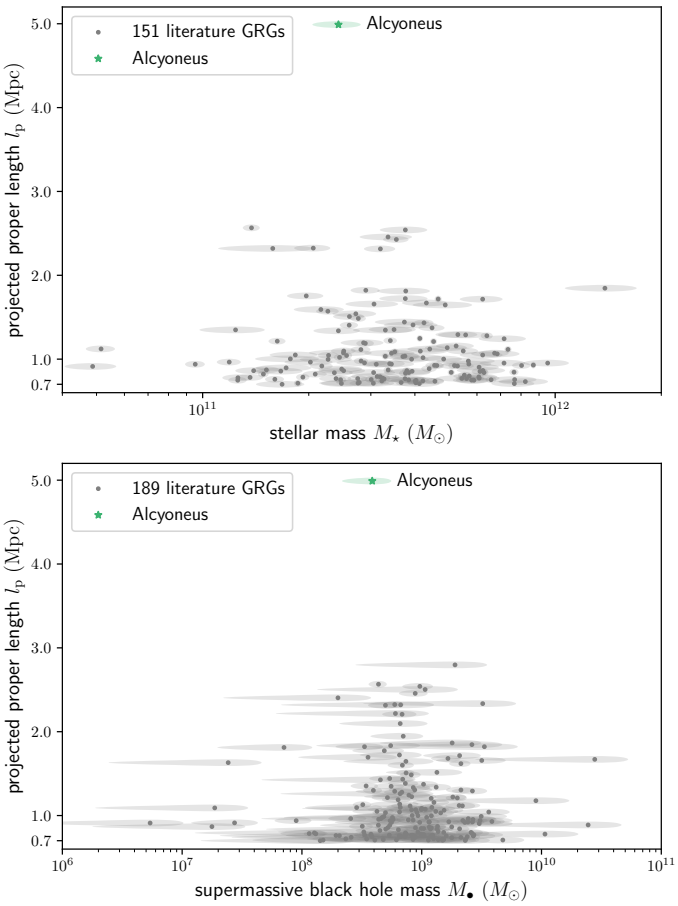

Fig. 7. Relations between the GRG projected proper length $l_{\rm p}$ and the host galaxy stellar mass $M_\star$ (*top panel*) and between the GRG $l_{\rm p}$ and the host galaxy SMBH mass $M_\bullet$ (*bottom panel*). Our methods allow these properties to be determined for a small proportion of all literature GRGs only. Literature GRGs are marked with grey disks, and Alcyoneus is marked with a green star. Translucent ellipses indicate −1 to +1 standard deviation uncertainties. Alcyoneus's host has a below-average stellar mass (percentile 25 ± 9%) and SMBH mass (percentile 23 ± 11%).

We note that Alcyoneus is the only GRG with $l_{\rm p} > 3$ Mpc whose host's stellar mass is known through Chang et al. (2015) or Salim et al. (2018), and whose host's SMBH mass can be estimated through its SDSS DR12 velocity dispersion. These data allow us to state confidently that exceptionally high stellar or SMBH masses are not necessary to generate 5-megaparsec-scale GRGs.

3.8. Surrounding large-scale structure

Several approaches to large-scale structure (LSS) classification, such as the T-web scheme (Hahn et al. 2007), partition the modern Universe into galaxy clusters, filaments, sheets, and voids. In this section, we determine Alcyoneus's most likely environment type using the SDSS DR7 spectroscopic galaxy sample (Abazajian et al. 2009).

In particular, we determined if Alcyoneus's host has fewer, about equal, or more galactic neighbours in SDSS DR7 than a randomly drawn galaxy of similar r-band luminosity density and redshift. Let $r(z)$ be the co-moving radial distance corresponding to cosmological redshift z. We considered a spherical shell with

[6] Taking $\beta_{\rm max} = 1$ instead, θ is bounded from above by $\theta_{\rm max} = 83.9 \pm 2°$ ($\theta \in [0, 90°]$), or bounded from below by $180° - \theta_{\rm max} = 96.1 \pm 2°$ ($\theta \in [90°, 180°]$).

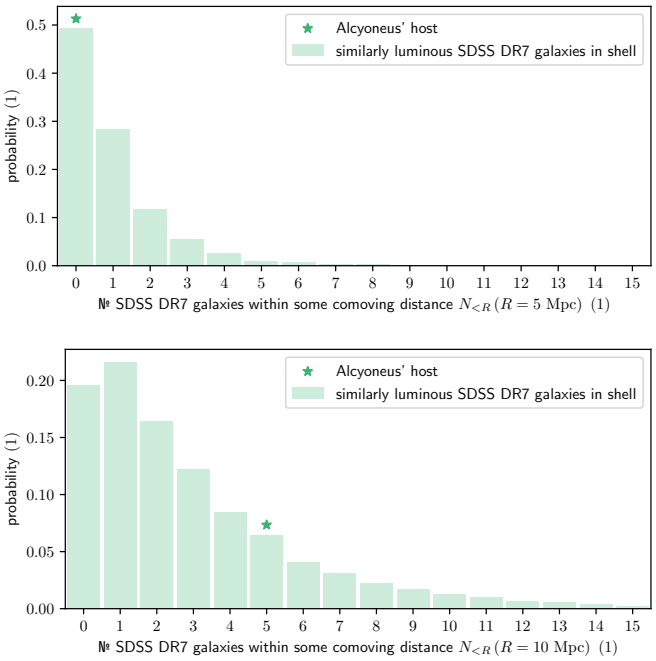

Fig. 8. Probability mass functions tracing the environmental density distribution of luminous galaxies at Alcyoneus's redshift. Like most galaxies of similar r-band luminosity density and redshift, Alcyoneus's host has no galactic neighbours in SDSS DR7 within 5 Mpc. However, within 10 Mpc, Alcyoneus's host has more neighbours than most similar galaxies. For all 9358 SDSS DR7 galaxies with an r-band luminosity density between 75% and 125% that of Alcyoneus's host and a co-moving radial distance that differs by at most $r_0 = 25$ Mpc from that of Alcyoneus, we count the number of SDSS DR7 galaxies, $N_{<R}(R)$, within a sphere of co-moving radius $R = 5$ Mpc (*top panel*) and $R = 10$ Mpc (*bottom panel*). The *top panel* indicates that Alcyoneus does not inhabit a galaxy cluster; the *bottom panel* indicates that Alcyoneus does not inhabit a void.

the observer at the centre, inner radius $\max\{r(z = z_{\mathrm{spec}}) - r_0, 0\}$ and outer radius $r(z = z_{\mathrm{spec}}) + r_0$. We approximated Alcyoneus's cosmological redshift with z_{spec} and chose $r_0 = 25$ Mpc. As all galaxies in the spherical shell have a similar distance to the observer (i.e. distances are at most $2r_0$ different), the SDSS DR7 galaxy number density completeness must also be similar throughout the spherical shell[7]. For each enclosed galaxy with an r-band luminosity density between $1 - \delta$ and $1 + \delta$ times that of Alcyoneus's host, we counted the number of SDSS DR7 galaxies $N_{<R}(R)$ within a sphere of co-moving radius R around it – regardless of luminosity density, and excluding itself. Alcyoneus's host has an SDSS r-band apparent magnitude $m_r = 18.20$; the corresponding luminosity density is $L_\nu(\lambda_c = 623.1\ \mathrm{nm}) = 3.75 \times 10^{22}$ W Hz^{-1}. We chose $\delta = 0.25$; this yielded 9,358 such enclosed galaxies.

In Fig. 8, we show the distribution of $N_{<R}(R)$ for $R = 5$ Mpc and $R = 10$ Mpc.

We verify that the distributions are insensitive to reasonable changes in r_0 and δ. We note that there is no SDSS DR7 galaxy within a co-moving distance of 5 Mpc from Alcyoneus's host. The nearest such galaxy, J081323.49+524856.1, occurs at a co-moving distance of 7.9 Mpc: the nearest ∼2000 Mpc^3 of co-moving space are free of galactic neighbours with $L_\nu(\lambda_c) > 5.57 \times 10^{22}$ W Hz^{-1}.[8] In the same way as in Sect. 3.1, we verified that the DESI Legacy Imaging Surveys DR9, RASS and PSZ2 do not contain evidence for a galaxy cluster in the direction of Alcyoneus's host. The nearest galaxy cluster, according to the SDSS-III cluster catalogue of Wen et al. (2012), instead lies 24″ away at right ascension 123.19926°, declination 52.72468° and photometric redshift $z_{\mathrm{ph}} = 0.2488$. It has an $R_{200} = 1.1$ Mpc and, according to the DESI cluster catalogue of Zou et al. (2021), a total mass $M = 2.2 \times 10^{14}\ M_\odot$. The co-moving distance between the cluster and Alcyoneus's host is 11 Mpc. All in all, we conclude that Alcyoneus does not reside in a galaxy cluster. Meanwhile, there are five SDSS DR7 galaxies within a co-moving distance of 10 Mpc from Alcyoneus's host: this makes it implausible that Alcyoneus lies in a void. Finally, one could interpret $N_{<R}(R)$ as a proxy for the LSS total matter density around a galaxy. For $R = 10$ Mpc, just 17% of galaxies in the shell with a similar luminosity density as Alcyoneus's host have a higher LSS total matter density. Being on the high end of the density distribution, but lying outside a cluster, Alcyoneus most probably inhabits a filament of the Cosmic Web.

3.9. Proper lobe volumes

We determined the proper volumes of Alcyoneus's lobes with a new Bayesian model. The model describes the lobes through a pair of doubly truncated, optically thin cones, each of which has a spatially constant and isotropic monochromatic emission coefficient (MEC; Rybicki & Lightman 1986). We allowed the 3D orientations and opening angles of the cones to differ, as the lobes can traverse their way through differently pressured parts of the warm–hot inter-galactic medium (WHIM): for example, the medium near the filament axis and the medium near the surrounding voids. By adopting a spatially constant MEC, we neglected electron density and magnetic field inhomogeneities as well as spectral-ageing gradients; by adopting an isotropic MEC, we assumed non-relativistic velocities within the lobe so that beaming effects are negligible. Numerically, we first generated the GRG's 3D MEC field over a cubical voxel grid, and then calculated the corresponding model image through projection, including expansion-related cosmological effects. Before comparison with the observed image, we convolved the model image with a Gaussian kernel to the appropriate resolution. We exploited the approximately Gaussian LoTSS DR2 image noise to formulate the likelihood, and assumed a flat prior distribution over the parameters. Using Metropolis–Hastings (MH) Markov chain Monte Carlo (MCMC), we sampled from the posterior distribution[9].

In the top panel of Fig. 9, we show the LoTSS DR2 compact-source-subtracted 90″ image of Alcyoneus. The central region has been excluded from source subtraction, and hence Alcyoneus's core and jets remain. (However, when we run our MH MCMC on this image, we do mask this central region.) In the middle panel, we show the highest-likelihood (and thus maximum a posteriori (MAP)) model image before convolution. In the bottom panel, we show the same model image convolved to 90″ resolution, with 2σ and 3σ contours of the observed image overlaid. We provide the full parameter set that corresponds with this model in Table C.1.

[7] For $r_0 = 25$ Mpc, this is a good approximation, because the shell is cosmologically thin: $2r_0 = 50$ Mpc roughly amounts to the length of a single Cosmic Web filament.

[8] This is the luminosity density that corresponds to the SDSS r-band apparent magnitude completeness limit $m_r = 17.77$ (Strauss et al. 2002).

[9] A detailed description of the model parameters, the MH MCMC, and the formulae for the derived quantities are given in Appendix C.

The posterior mean, calculated through the MH MCMC samples after burn-in, suggests the following geometry. The northern lobe has an opening angle $\gamma_1 = 10 \pm 1°$, and the cone truncates at an inner distance $d_{\mathrm{i},1} = 2.6 \pm 0.2$ Mpc and at an outer distance $d_{\mathrm{o},1} = 4.0 \pm 0.2$ Mpc from the host galaxy. The southern lobe has a larger opening angle $\gamma_2 = 26 \pm 2°$, but its cone truncates at smaller distances of $d_{\mathrm{i},2} = 1.5 \pm 0.1$ Mpc and $d_{\mathrm{o},2} = 2.0 \pm 0.1$ Mpc from the host galaxy. These parameters fix the proper volumes of Alcyoneus's northern and southern lobes. We find $V_1 = 1.5 \pm 0.2$ Mpc^3 and $V_2 = 1.0 \pm 0.2$ Mpc^3, respectively (see Eq. (C.15))[10].

Regarding the orientation of the lobes, Fig. 1 provides a visual hint that the lobes are subtly non-coaxial. The posterior indicates that the position angles of the northern and southern lobes are $\varphi_1 = 307 \pm 1°$ and $\varphi_2 = 139 \pm 2°$, respectively. The position angle difference is thus $\Delta\varphi = 168 \pm 2°$: although close to $\Delta\varphi = 180°$, we can reject the null hypothesis of coaxiality with high significance. Interestingly, the posterior also constrains the angles that the lobe axes make with the plane of the sky: $|\theta_1 - 90°| = 51 \pm 2°$ and $|\theta_2 - 90°| = 18 \pm 7°$. Again, the uncertainties imply that the lobes are probably not coaxial. We stress that these inclination angle results are tentative only. Future model extensions should explore how sensitive they are to the assumed lobe geometry (by testing other shapes than just truncated cones, such as ellipsoids).

One way to validate the model is to compare the observed lobe flux densities of Sect. 3.5 to the predicted lobe flux densities. According to the posterior, the MECs of the northern and southern lobes are $j_{\nu,1} = 17 \pm 2$ Jy deg^{-2} Mpc^{-1} and $j_{\nu,2} = 18 \pm 3$ Jy deg^{-2} Mpc^{-1}. Combining MECs and volumes, we predict northern and southern lobe flux densities $F_{\nu,1}(\nu_c) = 63 \pm 4$ mJy and $F_{\nu,2}(\nu_c) = 45 \pm 5$ mJy (see Eq. (C.16)). We find excellent agreement: the relative differences with the observed results are 0% and 2%, respectively.

3.10. Lobe pressures and the local WHIM

From Alcyoneus's lobe flux densities and volumes, we can infer lobe pressures and magnetic field strengths. We calculated these through `pysynch`[11] (Hardcastle et al. 1998b), which uses the formulae first proposed by Myers & Spangler (1985) and reexamined by Beck & Krause (2005). Following the notation of Hardcastle et al. (1998b), we assumed that the electron energy distribution is a power law in Lorentz factor γ with $\gamma_{\mathrm{min}} = 10$, $\gamma_{\mathrm{max}} = 10^4$ and exponent $p = -2$; we also assumed that the kinetic energy density of protons is vanishingly small compared with that of electrons ($\kappa = 0$) and that the plasma filling factor is unity ($\phi = 1$). Assuming the minimum-energy condition (Burbidge 1956), we find minimum-energy pressures $P_{\mathrm{min},1} = 4.8 \pm 0.3 \times 10^{-16}$ Pa and $P_{\mathrm{min},2} = 4.9 \pm 0.6 \times 10^{-16}$ Pa for the northern and southern lobes, respectively. The corresponding minimum-energy magnetic field strengths are $B_{\mathrm{min},1} = 46 \pm 1$ pT and $B_{\mathrm{min},2} = 46 \pm 3$ pT. Assuming the equipartition condition (Pacholczyk 1970), we find equipartition pressures $P_{\mathrm{eq},1} = 4.9 \pm 0.3 \times 10^{-16}$ Pa and $P_{\mathrm{eq},2} = 4.9 \pm 0.6 \times 10^{-16}$ Pa for the northern and southern lobes, respectively. The corresponding equipartition magnetic field strengths are $B_{\mathrm{eq},1} = 43 \pm 2$ pT and

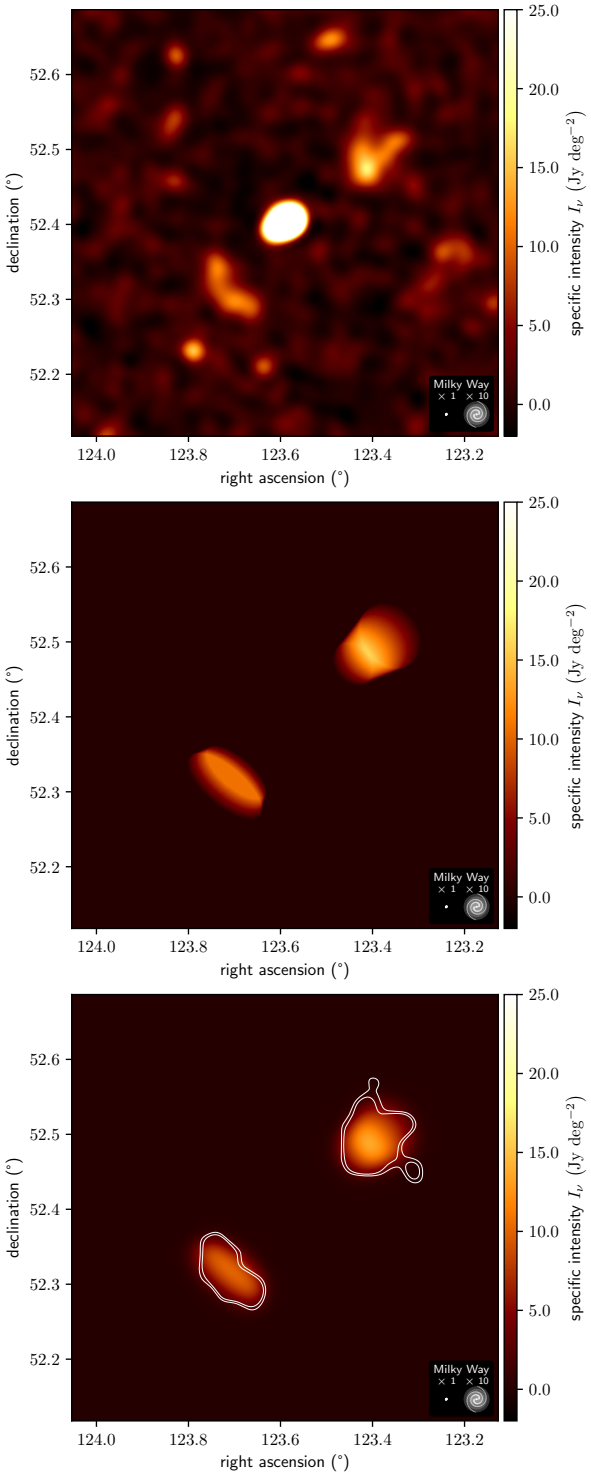

Fig. 9. Bayesian model overview, showing how Alcyoneus's lobe volumes can be estimated by comparing an observed radio image to modelled radio images. *Top*: LoTSS DR2 compact-source-subtracted 90″ image of Alcyoneus. *Middle*: highest-likelihood model image. *Bottom*: same model image convolved to 90″ resolution, with 2σ and 3σ contours of the observed image overlaid.

[10] As a sanity check, we compared our results to those from a less rigorous, though simpler, ellipsoid-based method of estimating volumes. By fitting ellipses to the image in the top panel of Fig. 9, one obtains a semi-minor and semi-major axis; the half-diameter along the ellipsoid's third dimension is assumed to be their mean. This method suggests a northern lobe volume $V_1 = 1.4 \pm 0.3$ Mpc^3 and a southern lobe volume $V_2 = 1.1 \pm 0.3$ Mpc^3. These results agree well with our Bayesian model results. (If the half-diameter along the third dimension is instead treated as an RV with a uniform distribution between the semi-minor axis and the semi-major axis, the estimates remain the same.)

[11] The `pysynch` code is publicly available online: https://github.com/mhardcastle/pysynch.

$B_{\rm eq,2} = 43 \pm 2$ pT. The minimum-energy and equipartition results do not differ significantly.

From pressures and volumes, we estimated the internal energy of the lobes $E = 3PV$. We find $E_{\rm min,1} = 6.2 \pm 0.5 \times 10^{52}$ J, $E_{\rm min,2} = 4.3 \pm 0.6 \times 10^{52}$ J, $E_{\rm eq,1} = 6.3 \pm 0.5 \times 10^{52}$ J and $E_{\rm eq,2} = 4.4 \pm 0.6 \times 10^{52}$ J. Next, we could bound the ages of the lobes from below by neglecting synchrotron losses and assuming that the jets have been injecting energy in the lobes continuously at the currently observed kinetic jet powers. Using $\Delta t = EQ_{\rm jet}^{-1}$, we find $\Delta t_{\rm min,1} = 1.7 \pm 0.2$ Gyr, $\Delta t_{\rm min,2} = 2.1 \pm 0.4$ Gyr, and identical results when assuming the equipartition condition. Finally, we could obtain a rough estimate of the average expansion speed of the RG during its lifetime $u = l_{\rm p}(\Delta t)^{-1}$. We find $u = 2.6 \pm 0.3 \times 10^3$ km s^{-1}, or about 1% of the speed of light.

Several other authors (Andernach et al. 1992; Lacy et al. 1993; Subrahmanyan et al. 1996, 2006, 2008; Parma et al. 1996; Mack et al. 1998; Schoenmakers et al. 1998, 2000; Ishwara-Chandra & Saikia 1999; Lara et al. 2000; Machalski & Jamrozy 2000; Machalski et al. 2001, 2006, 2007, 2008; Saripalli et al. 2002; Jamrozy et al. 2005; Saikia et al. 2006; Safouris et al. 2009; Malarecki et al. 2013; Tamhane et al. 2015; Sebastian et al. 2018; Heesen et al. 2018; Cantwell et al. 2020) have estimated the minimum-energy or equipartition pressure of the lobes of GRGs embedded in non-cluster environments (i.e. in voids, sheets or filaments of the Cosmic Web). We compare Alcyoneus to the other 151 GRGs with known lobe pressures in the top panel of Fig. 10.[12] Alcyoneus reaffirms the negative correlation between length and lobe pressure (Jamrozy & Machalski 2002; Machalski & Jamrozy 2006), and it has the lowest lobe pressures found thus far. Alcyoneus's lobe pressures are in fact so low that they are comparable to the pressure in dense and hot parts of the WHIM: for a baryonic matter (BM) density $\rho_{\rm WHIM} = 10\,\rho_{\rm c,0}\Omega_{\rm BM,0}$ and $T_{\rm WHIM} = 10^7$ K, $P_{\rm WHIM} = 4 \times 10^{-16}$ Pa. Here, $\rho_{\rm c,0}$ is today's critical density, so $\rho_{\rm c,0}\Omega_{\rm BM,0}$ is today's mean baryon density. A more extensive comparison between $P_{\rm min}$ (green line) and $P_{\rm WHIM}$ (red lines) is shown in the bottom panel of Fig. 10. For comparison, we also show the lobe pressures of the four other thus-analysed GRGs with $l_{\rm p} > 3$ Mpc (grey lines). These are J1420−0545 of $l_{\rm p} = 4.9$ Mpc (Machalski et al. 2008), 3C 236 of $l_{\rm p} = 4.7$ Mpc (Schoenmakers et al. 2000), J0331−7710 of $l_{\rm p} = 3.4$ Mpc (Malarecki et al. 2013) and B2147+816 of $l_{\rm p} = 3.1$ Mpc (Schoenmakers et al. 2000).

Although proposed as probes of WHIM thermodynamics for decades, the bottom panel of Fig. 10 demonstrates that even the largest non-cluster literature GRGs are unlikely to be in pressure equilibrium with their environment. Relying on results from the Overwhelmingly Large Simulations (OWLS; Schaye et al. 2010), Malarecki et al. (2013) point out that baryon densities $\rho_{\rm BM} > 50\,\rho_{\rm c,0}\,\Omega_{\rm BM,0}$, which are necessary for pressure equilibrium in these GRGs (see the intersection of grey and red lines in the bottom panel of Fig. 10), occur in only 1% of the WHIM's volume. By contrast, Alcyoneus can be in pressure equilibrium with the WHIM at baryon densities $\rho_{\rm BM} \sim 20\,\rho_{\rm c,0}\,\Omega_{\rm BM,0}$ and, thus, represents the most promising inter-galactic barometer of its kind yet[13].

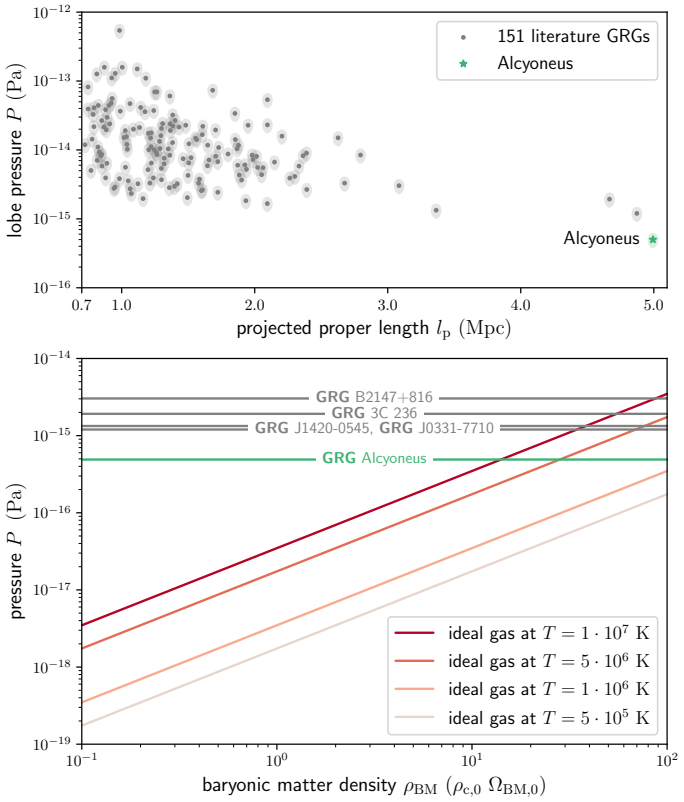

Fig. 10. Panels showing that, of all GRGs with known lobe pressures, Alcyoneus is the most plausible candidate for pressure equilibrium with the WHIM. *Top panel*: we explore the relation between length and lobe pressure for Alcyoneus and 151 literature GRGs. *Bottom panel*: we compare the lobe pressure of Alcyoneus (green line) with WHIM pressures (red lines). For reference, we also show the lobe pressures of the four largest similarly analysed GRGs (grey lines).

A final question is why most, if not all, observed non-cluster GRGs have over-pressured lobes. The top panel of Fig. 10 suggests that GRGs must grow to several megaparsecs to approach WHIM pressures in their lobes, and such GRGs are rare. However, the primary reason is the limited surface brightness sensitivity of all past and current surveys. Alcyoneus's lobes are visible in the LoTSS, but not in the NRAO VLA Sky Survey (NVSS; Condon et al. 1998) or in the Westerbork Northern Sky Survey (WENSS; Rengelink et al. 1997). Their pressures approach that of the bulk of the WHIM within an order of magnitude. Lobes with even lower pressure must be less luminous or more voluminous, and thus will have even lower surface brightness. It is therefore probable that most GRG lobes that are in true pressure equilibrium with the WHIM still lie hidden in the radio sky.

4. Conclusion

In this work, we have presented the discovery of a radio galaxy of at least 5 Mpc. We have measured its key physical characteristics, and explored possible reasons for its exceptional growth.

1. We reprocessed the LoTSS DR2, the latest version of the LOFAR's northern sky survey at 144 MHz, by subtracting angularly compact sources and imaging at 60″ and

[12] We have included all publications that provide pressures, energy densities or magnetic field strengths. We note that some authors assumed $\gamma_{\rm min} = 1$, we assumed $\gamma_{\rm min} = 10$ and Malarecki et al. (2013) assumed $\gamma_{\rm min} = 10^3$. If possible, angular lengths were updated using the LoTSS DR2 at 6″ and redshift estimates were updated using the SDSS DR12. All projected proper lengths have been recalculated using our Planck Collaboration VI (2020) cosmology. When authors provided pressures for both lobes, we have taken the average.

[13] At Alcyoneus's redshift, this density amounts to a baryon overdensity of ∼10.

90″ resolution. The resulting images Oei et al. (in prep.) allow us to explore a new sensitivity regime for RG lobes and thus represent promising data to search for unknown GRGs of large angular length. We will present a sample in forthcoming work.

2. We have discovered the first 5 Mpc GRG, which we dub 'Alcyoneus'. The projected proper length is $l_{\rm p} = 4.99 \pm 0.04$ Mpc, while the true proper length is at least $l_{\rm min} = 5.04 \pm 0.05$ Mpc. We confidently associate the $20.8' \pm 0.15'$ radio structure with an elliptical galaxy with a jet-mode AGN detected in the DESI Legacy Imaging Surveys DR9: the SDSS DR12 source J081421.68+522410.0 at J2000 right ascension 123.590372°, declination 52.402795°, and spectroscopic redshift $0.24674 \pm 6 \times 10^{-5}$.
3. Alcyoneus has a total luminosity density at $\nu = 144$ MHz of $L_\nu = 8 \pm 1 \times 10^{25}$ W Hz^{-1}, which is typical for GRGs (percentile $45 \pm 3\%$). Alcyoneus's host has a fairly low stellar mass and SMBH mass compared with other GRG hosts (percentiles $25 \pm 9\%$ and $23 \pm 11\%$). This implies that – within the GRG population – no strong positive correlation between RG length and (instantaneous) low-frequency radio power, stellar mass, or SMBH mass can exist.
4. A poly-chromatic examination of the surrounding sky – using the RASS, the DESI Legacy Imaging Surveys DR9, the PSZ2, and the LoTSS DR2 – suggests that Alcyoneus does not inhabit a galaxy cluster.
   According to an SDSS-III cluster catalogue, the nearest cluster occurs at a co-moving distance of 11 Mpc. A local galaxy number density count suggests that Alcyoneus instead inhabits a filament of the Cosmic Web. A low-density environment therefore remains a possible explanation for Alcyoneus's formidable size.
5. We have developed a new Bayesian model that parametrises in three dimensions a pair of arbitrarily oriented, optically thin, doubly truncated conical RG lobes with a constant MEC. We then generated the corresponding specific intensity function, taking cosmic expansion into account, and compared it to data, assuming Gaussian image noise. We used MH MCMC to optimise the parameters and thus determined northern and southern lobe volumes of 1.5 ± 0.2 Mpc^3 and 1.0 ± 0.2 Mpc^3, respectively. In total, the lobes have an internal energy of $\sim 10^{53}$ J, expelled from the host galaxy over a gigayear-scale period.
   The lobe pressures are $4.8 \pm 0.3 \times 10^{-16}$ Pa and $4.9 \pm 0.6 \times 10^{-16}$ Pa, respectively; these are the lowest measured in radio galaxies yet. Nevertheless, the lobe pressures still exceed a large range of plausible WHIM pressures. Most likely, the lobes are still expanding – and Alcyoneus's struggle for supremacy of the cosmos continues.

Acknowledgements. M.S.S.L. Oei warmly thanks Frits Sweijen for coding the very useful https://github.com/tikk3r/legacystamps. M.S.S.L. Oei, R.J. van Weeren and A. Botteon acknowledge support from the VIDI research programme with project number 639.042.729, which is financed by The Netherlands Organisation for Scientific Research (NWO). M. Brüggen acknowledges support from the Deutsche Forschungsgemeinschaft under Germany's Excellence Strategy – EXC 2121 'Quantum Universe' – 390833306. W.L. Williams acknowledges support from the CAS–NWO programme for radio astronomy with project number 629.001.024, which is financed by The Netherlands Organisation for Scientific Research (NWO). The LOFAR is the Low-Frequency Array designed and constructed by ASTRON. It has observing, data processing, and data storage facilities in several countries, which are owned by various parties (each with their own funding sources), and which are collectively operated by the ILT Foundation under a joint scientific policy. The ILT resources have benefited from the following recent major funding sources: CNRS–INSU, Observatoire de Paris and Université d'Orléans, France; BMBF, MIWF–NRW, MPG, Germany; Science Foundation Ireland (SFI), Department of Business, Enterprise and Innovation (DBEI), Ireland; NWO, The Netherlands; the Science and Technology Facilities Council, UK; Ministry of Science and Higher Education, Poland; the Istituto Nazionale di Astrofisica (INAF), Italy. The National Radio Astronomy Observatory is a facility of the National Science Foundation operated under cooperative agreement by Associated Universities, Inc. CIRADA is funded by a grant from the Canada Foundation for Innovation 2017 Innovation Fund (Project 35999), as well as by the Provinces of Ontario, British Columbia, Alberta, Manitoba and Quebec. Funding for SDSS-III has been provided by the Alfred P. Sloan Foundation, the Participating Institutions, the National Science Foundation, and the U.S. Department of Energy Office of Science. The SDSS-III web site is http://www.sdss3.org/. SDSS-III is managed by the Astrophysical Research Consortium for the Participating Institutions of the SDSS-III Collaboration including the University of Arizona, the Brazilian Participation Group, Brookhaven National Laboratory, Carnegie Mellon University, University of Florida, the French Participation Group, the German Participation Group, Harvard University, the Instituto de Astrofisica de Canarias, the Michigan State/Notre Dame/JINA Participation Group, Johns Hopkins University, Lawrence Berkeley National Laboratory, Max Planck Institute for Astrophysics, Max Planck Institute for Extraterrestrial Physics, New Mexico State University, New York University, Ohio State University, Pennsylvania State University, University of Portsmouth, Princeton University, the Spanish Participation Group, University of Tokyo, University of Utah, Vanderbilt University, University of Virginia, University of Washington, and Yale University. The Pan-STARRS1 Surveys (PS1) and the PS1 public science archive have been made possible through contributions by the Institute for Astronomy, the University of Hawaii, the Pan-STARRS Project Office, the Max-Planck Society and its participating institutes, the Max Planck Institute for Astronomy, Heidelberg and the Max Planck Institute for Extraterrestrial Physics, Garching, The Johns Hopkins University, Durham University, the University of Edinburgh, the Queen's University Belfast, the Harvard-Smithsonian Center for Astrophysics, the Las Cumbres Observatory Global Telescope Network Incorporated, the National Central University of Taiwan, the Space Telescope Science Institute, the National Aeronautics and Space Administration under Grant No. NNX08AR22G issued through the Planetary Science Division of the NASA Science Mission Directorate, the National Science Foundation Grant No. AST-1238877, the University of Maryland, Eotvos Lorand University (ELTE), the Los Alamos National Laboratory, and the Gordon and Betty Moore Foundation. This publication makes use of data products from the Wide-Field Infrared Survey Explorer, which is a joint project of the University of California, Los Angeles, and the Jet Propulsion Laboratory/California Institute of Technology, funded by the National Aeronautics and Space Administration. The Legacy Surveys consist of three individual and complementary projects: the Dark Energy Camera Legacy Survey (DECaLS; Proposal ID #2014B-0404; PIs: David Schlegel and Arjun Dey), the Beijing–Arizona Sky Survey (BASS; NOAO Prop. ID #2015A-0801; PIs: Zhou Xu and Xiaohui Fan), and the Mayall z-band Legacy Survey (MzLS; Prop. ID #2016A-0453; PI: Arjun Dey). DECaLS, BASS and MzLS together include data obtained, respectively, at the Blanco telescope, Cerro Tololo Inter-American Observatory, NSF's NOIRLab; the Bok telescope, Steward Observatory, University of Arizona; and the Mayall telescope, Kitt Peak National Observatory, NOIRLab. The Legacy Surveys project is honored to be permitted to conduct astronomical research on Iolkam Du'ag (Kitt Peak), a mountain with particular significance to the Tohono O'odham Nation. NOIRLab is operated by the Association of Universities for Research in Astronomy (AURA) under a cooperative agreement with the National Science Foundation. This project used data obtained with the Dark Energy Camera (DECam), which was constructed by the Dark Energy Survey (DES) collaboration. Funding for the DES Projects has been provided by the U.S. Department of Energy, the U.S. National Science Foundation, the Ministry of Science and Education of Spain, the Science and Technology Facilities Council of the United Kingdom, the Higher Education Funding Council for England, the National Center for Supercomputing Applications at the University of Illinois at Urbana-Champaign, the Kavli Institute of Cosmological Physics at the University of Chicago, Center for Cosmology and Astro-Particle Physics at the Ohio State University, the Mitchell Institute for Fundamental Physics and Astronomy at Texas A&M University, Financiadora de Estudos e Projetos, Fundacao Carlos Chagas Filho de Amparo, Financiadora de Estudos e Projetos, Fundacao Carlos Chagas Filho de Amparo a Pesquisa do Estado do Rio de Janeiro, Conselho Nacional de Desenvolvimento Cientifico e Tecnologico and the Ministerio da Ciencia, Tecnologia e Inovacao, the Deutsche Forschungsgemeinschaft and the Collaborating Institutions in the Dark Energy Survey. The Collaborating Institutions are Argonne National Laboratory, the University of California at Santa Cruz, the University of Cambridge, Centro de Investigaciones Energeticas, Medioambientales y Tecnologicas-Madrid, the University of Chicago, University College London, the DES-Brazil Consortium, the University of Edinburgh, the Eidgenössische Technische Hochschule (ETH) Zürich, Fermi National Accelerator Laboratory, the University of Illinois at Urbana-Champaign, the Institut de Ciencies de l'Espai (IEEC/CSIC), the Institut de Fisica d'Altes Energies, Lawrence Berkeley National Laboratory, the Ludwig Maximilians

Universität München and the associated Excellence Cluster Universe, the University of Michigan, NSF's NOIRLab, the University of Nottingham, the Ohio State University, the University of Pennsylvania, the University of Portsmouth, SLAC National Accelerator Laboratory, Stanford University, the University of Sussex, and Texas A&M University. BASS is a key project of the Telescope Access Program (TAP), which has been funded by the National Astronomical Observatories of China, the Chinese Academy of Sciences (the Strategic Priority Research Program "The Emergence of Cosmological Structures" Grant # XDB09000000), and the Special Fund for Astronomy from the Ministry of Finance. The BASS is also supported by the External Cooperation Program of Chinese Academy of Sciences (Grant # 114A11KYSB20160057), and Chinese National Natural Science Foundation (Grant # 11433005). The Legacy Survey team makes use of data products from the Near-Earth Object Wide-Field Infrared Survey Explorer (NEOWISE), which is a project of the Jet Propulsion Laboratory/California Institute of Technology. NEOWISE is funded by the National Aeronautics and Space Administration. The Legacy Surveys imaging of the DESI footprint is supported by the Director, Office of Science, Office of High Energy Physics of the U.S. Department of Energy under Contract No. DE-AC02-05CH1123, by the National Energy Research Scientific Computing Center, a DOE Office of Science User Facility under the same contract; and by the U.S. National Science Foundation, Division of Astronomical Sciences under Contract No. AST-0950945 to NOAO.

References

Abazajian, K. N., Adelman-McCarthy, J. K., Agüeros, M. A., et al. 2009, ApJS, 182, 543
Alam, S., Albareti, F. D., Prieto, C. A., et al. 2015, ApJS, 219, 12
Andernach, H., Feretti, L., Giovannini, G., et al. 1992, A&AS, 93, 331
Andernach, H., Jiménez-Andrade, E. F., & Willis, A. G. 2021, Galaxies, 9, 99
Bassani, L., Ursini, F., Malizia, A., et al. 2021, MNRAS, 500, 3111
Beck, R., & Krause, M. 2005, Astron. Nachr., 326, 414
Best, P. N., & Heckman, T. M. 2012, MNRAS, 421, 1569
Best, P. N., Ker, L. M., Simpson, C., Rigby, E. E., & Sabater, J. 2014, MNRAS, 445, 955
Blandford, R. D., & Rees, M. J. 1974, MNRAS, 169, 395
Bonnarel, F., Fernique, P., Bienaymé, O., et al. 2000, A&AS, 143, 33
Boxelaar, J. M., van Weeren, R. J., & Botteon, A. 2021, Astron. Comput., 35, 100464
Brüggen, M., Reiprich, T. H., Bulbul, E., et al. 2021, A&A, 647, A3
Burbidge, G. R. 1956, ApJ, 124, 416
Cantwell, T. M., Bray, J. D., Croston, J. H., et al. 2020, MNRAS, 495, 143
Chambers, K. C., Magnier, E. A., Metcalfe, N., et al. 2016, ArXiv e-prints [arXiv:1612.05560]
Chang, Y.-Y., van der Wel, A., da Cunha, E., & Rix, H.-W. 2015, ApJS, 219, 8
Condon, J. J., Cotton, W. D., Greisen, E. W., et al. 1998, AJ, 115, 1693
Condon, J. J., Cotton, W. D., Fomalont, E. B., et al. 2012, ApJ, 758, 23
Cutri, R. M., Skrutskie, M. F., van Dyk, S., et al. 2012, VizieR Online Data Catalog: II/311
Dabhade, P., Mahato, M., Bagchi, J., et al. 2020a, A&A, 642, A153
Dabhade, P., Röttgering, H. J. A., Bagchi, J., et al. 2020b, A&A, 635, A5
Delhaize, J., Heywood, I., Prescott, M., et al. 2021, MNRAS, 501, 3833
Dey, A., Schlegel, D. J., Lang, D., et al. 2019, AJ, 157, 168
Galvin, T. J., Huynh, M. T., Norris, R. P., et al. 2020, MNRAS, 497, 2730
Gürkan, G., Hardcastle, M. J., & Jarvis, M. J. 2014, MNRAS, 438, 1149
Hahn, O., Porciani, C., Carollo, C. M., & Dekel, A. 2007, MNRAS, 375, 489
Hardcastle, M. J. 2018, MNRAS, 475, 2768
Hardcastle, M. J., & Croston, J. H. 2020, New Astron. Rev., 88, 101539
Hardcastle, M. J., Alexander, P., Pooley, G. G., & Riley, J. M. 1998a, MNRAS, 296, 445
Hardcastle, M. J., Worrall, D. M., & Birkinshaw, M. 1998b, MNRAS, 296, 1098
Heckman, T. M., & Best, P. N. 2014, ARA&A, 52, 589
Heesen, V., Croston, J. H., Morganti, R., et al. 2018, MNRAS, 474, 5049
Ishwara-Chandra, C. H., & Saikia, D. J. 1999, MNRAS, 309, 100
Ishwara-Chandra, C. H., Taylor, A. R., Green, D. A., et al. 2020, MNRAS, 497, 5383
Jamrozy, M., & Machalski, J. 2002, in IAU Colloq. 184: AGN Surveys, eds. R. F. Green, E. Y. Khachikian, & D. B. Sanders, ASP Conf. Ser., 284, 295
Jamrozy, M., Machalski, J., Mack, K. H., & Klein, U. 2005, A&A, 433, 467
Jamrozy, M., Konar, C., Machalski, J., & Saikia, D. J. 2008, MNRAS, 385, 1286
Kormendy, J., & Ho, L. C. 2013, ARA&A, 51, 511
Kuminski, E., & Shamir, L. 2016, ApJS, 223, 20
Kuźmicz, A., & Jamrozy, M. 2021, ApJS, 253, 25
Kuźmicz, A., Jamrozy, M., Bronarska, K., Janda-Boczar, K., & Saikia, D. J. 2018, ApJS, 238, 9
Lacy, M., Rawlings, S., Saunders, R., & Warner, P. J. 1993, MNRAS, 264, 721
Lacy, M., Baum, S. A., Chandler, C. J., et al. 2020, PASP, 132, 035001
Laing, R. A., & Bridle, A. H. 2014, MNRAS, 437, 3405
Lara, L., Mack, K. H., Lacy, M., et al. 2000, A&A, 356, 63
Machalski, J. 2011, MNRAS, 413, 2429
Machalski, J., & Jamrozy, M. 2000, A&A, 363, L17
Machalski, J., & Jamrozy, M. 2006, A&A, 454, 95
Machalski, J., Jamrozy, M., & Zola, S. 2001, A&A, 371, 445
Machalski, J., Jamrozy, M., Zola, S., & Koziel, D. 2006, A&A, 454, 85
Machalski, J., Koziel-Wierzbowska, D., & Jamrozy, M. 2007, AcA, 57, 227
Machalski, J., Kozieł-Wierzbowska, D., Jamrozy, M., & Saikia, D. J. 2008, ApJ, 679, 149
Mack, K. H., Klein, U., O'Dea, C. P., Willis, A. G., & Saripalli, L. 1998, A&A, 329, 431
Mahato, M., Dabhade, P., Saikia, D. J., et al. 2022, A&A, in press, https://doi.org/10.1051/0004-6361/202141928
Malarecki, J. M., Staveley-Smith, L., Saripalli, L., et al. 2013, MNRAS, 432, 200
Masini, A., Celotti, A., Grandi, P., Moravec, E., & Williams, W. L. 2021, A&A, 650, A51
Myers, S. T., & Spangler, S. R. 1985, ApJ, 291, 52
Offringa, A. R., & Smirnov, O. 2017, MNRAS, 471, 301
Offringa, A. R., McKinley, B., Hurley-Walker, N., et al. 2014, MNRAS, 444, 606
Pacholczyk, A. G. 1970, Radio Astrophysics. Nonthermal Processes in Galactic and Extragalactic Sources (San Francisco: Freeman)
Parma, P., de Ruiter, H. R., Mack, K. H., et al. 1996, A&A, 311, 49
Planck Collaboration XXVII. 2016, A&A, 594, A27
Planck Collaboration VI. 2020, A&A, 641, A6
Pracy, M. B., Ching, J. H. Y., Sadler, E. M., et al. 2016, MNRAS, 460, 2
Rengelink, R. B., Tang, Y., de Bruyn, A. G., et al. 1997, A&AS, 124, 259
Ringermacher, H. I., & Mead, L. R. 2009, MNRAS, 397, 164
Rybicki, G. B., & Lightman, A. P. 1986, Radiative Processes in Astrophysics (Wiley-VCH)
Safouris, V., Subrahmanyan, R., Bicknell, G. V., & Saripalli, L. 2009, MNRAS, 393, 2
Saikia, D. J., Konar, C., & Kulkarni, V. K. 2006, MNRAS, 366, 1391
Salim, S., Boquien, M., & Lee, J. C. 2018, ApJ, 859, 11
Saripalli, L., Subrahmanyan, R., & Udaya Shankar, N. 2002, ApJ, 565, 256
Schaye, J., Dalla Vecchia, C., Booth, C. M., et al. 2010, MNRAS, 402, 1536
Schoenmakers, A. P., Mack, K. H., Lara, L., et al. 1998, A&A, 336, 455
Schoenmakers, A. P., Mack, K. H., de Bruyn, A. G., et al. 2000, A&AS, 146, 293
Scott, D., & Tout, C. A. 1989, MNRAS, 241, 109
Sebastian, B., Ishwara-Chandra, C. H., Joshi, R., & Wadadekar, Y. 2018, MNRAS, 473, 4926
Shimwell, T. W., Röttgering, H. J. A., Best, P. N., et al. 2017, A&A, 598, A104
Shimwell, T. W., Tasse, C., Hardcastle, M. J., et al. 2019, A&A, 622, A1
Shimwell, T., Hardcastle, M. J., Tasse, C., et al. 2022, A&A, 659, A1
Soltan, A. 1982, MNRAS, 200, 115
Strauss, M. A., Weinberg, D. H., Lupton, R. H., et al. 2002, AJ, 124, 1810
Subrahmanyan, R., Saripalli, L., & Hunstead, R. W. 1996, MNRAS, 279, 257
Subrahmanyan, R., Hunstead, R. W., Cox, N. L. J., & McIntyre, V. 2006, ApJ, 636, 172
Subrahmanyan, R., Saripalli, L., Safouris, V., & Hunstead, R. W. 2008, ApJ, 677, 63
Tamhane, P., Wadadekar, Y., Basu, A., et al. 2015, MNRAS, 453, 2438
Tang, H., Scaife, A. M. M., Wong, O. I., et al. 2020, MNRAS, 499, 68
Tasse, C., Hugo, B., Mirmont, M., et al. 2018, A&A, 611, A87
van der Tol, S., Veenboer, B., & Offringa, A. R. 2018, A&A, 616, A27
van Haarlem, M. P., Wise, M. W., Gunst, A. W., et al. 2013, A&A, 556, A2
van Weeren, R. J., Shimwell, T. W., Botteon, A., et al. 2021, A&A, 651, A115
Voges, W., Aschenbach, B., Boller, T., et al. 1999, A&A, 349, 389
Wen, Z. L., Han, J. L., & Liu, F. S. 2012, ApJS, 199, 34
Williams, W. L., Calistro Rivera, G., Best, P. N., et al. 2018, MNRAS, 475, 3429
Willis, A. G., Strom, R. G., & Wilson, A. S. 1974, Nature, 250, 625
Zou, H., Gao, J., Xu, X., et al. 2021, ApJS, 253, 56

Appendix A: J1420-0545 comparison

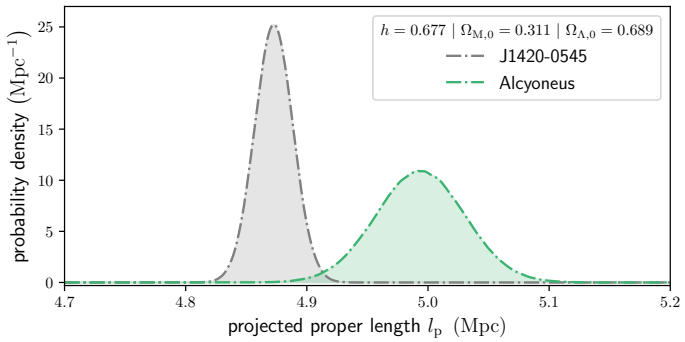

Fig. A.1. PDFs showing that Alcyoneus's projected proper length just exceeds that of J1420-0545. The probability that Alcyoneus (green) has a larger projected proper length than J1420-0545 (grey) (Machalski et al. 2008) is 99.9%. For both GRGs, we take into account uncertainty in angular length and spectroscopic redshift, as well as the possibility of peculiar motion along the line of sight.

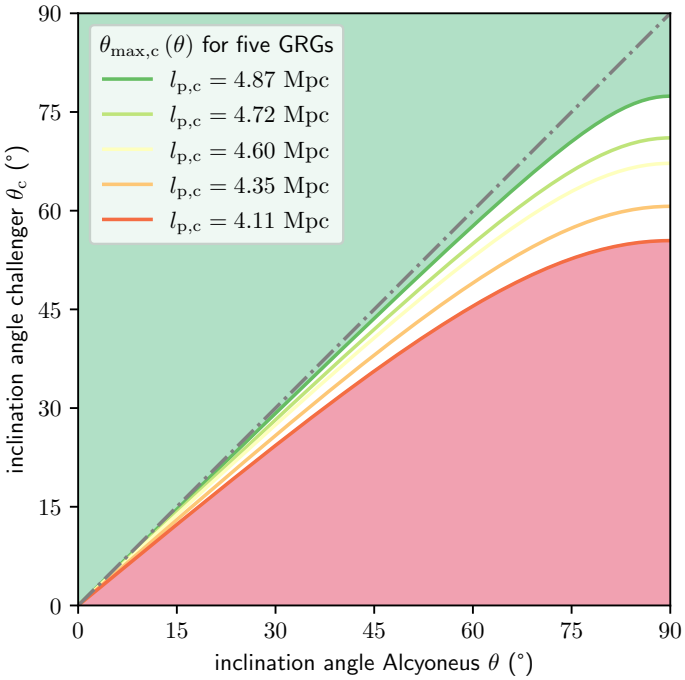

Fig. A.2. Schematic of conditions under which Alcyoneus is not only the longest GRG in the plane of the sky but also in three dimensions. Alcyoneus's inclination angle, θ, is not well determined, and therefore the full range of possibilities is shown on the horizontal axis. To surpass Alcyoneus in true proper length, challengers must have smaller inclination angles than Alcyoneus (i.e. appear below the dotted grey equality line). More specifically, as a function of θ, we show the inclination angle $\theta_{max,c}$ below which challengers with a projected proper length $l_{p,c} > 4$ Mpc trump Alcyoneus (coloured curves). The shaded areas of parameter space represent regimes with a particularly straightforward interpretation. One can imagine populating the graph with five points (located along the same vertical line), representing the ground-truth inclination angles of Alcyoneus and its five challengers. If any of these points fall in the red-shaded area, Alcyoneus is not the longest GRG in 3D. If all points fall in the green-shaded area, Alcyoneus is the longest GRG in 3D.

We verified that Alcyoneus is the longest known RG in projection by comparing it with J1420-0545 (Machalski et al. 2008), the literature's record holder.

The angular lengths of Alcyoneus and J1420-0545 are $\phi = 20.8' \pm 0.15'$ and $\phi = 17.4' \pm 0.05'$, respectively. For J1420-0545, we adopted the angular length reported by Machalski et al. (2008) because it lies outside the LoTSS DR2 coverage. The spectroscopic redshifts of Alcyoneus and J1420-0545 are $z_{spec} = 0.24674 \pm 6 \times 10^{-5}$ and $z_{spec} = 0.3067 \pm 5 \times 10^{-4}$, respectively. For both giants, we assumed the peculiar velocity along the line of sight u_p to be a Gaussian random variable (RV) with mean 0 and standard deviation 100 km s^{-1}, similar to conditions in low-mass galaxy clusters. (Both giants actually reside in filaments.)

Equations A.1 describe how to calculate the cosmological redshift RV z via the peculiar velocity redshift RV z_p:

$$\beta_p := \frac{u_p}{c}; \quad z_p = \sqrt{\frac{1+\beta_p}{1-\beta_p}} - 1; \quad z = \frac{1+z_{spec}}{1+z_p} - 1. \tag{A.1}$$

Here, c is the speed of light *in vacuo*. Finally, we calculated the projected proper length RV $l_p = r_\phi(z, \mathfrak{M}) \cdot \phi$. Here, r_ϕ is the angular diameter distance RV, which depends on cosmological model parameters $\mathfrak{M}$. Propagating the uncertainties in angular length ϕ, spectroscopic redshift z_{spec} and peculiar velocity along the line of sight u_p through Monte Carlo simulation, the projected proper lengths of Alcyoneus and J1420-0545 are $l_p = 4.99 \pm 0.04$ Mpc and $l_p = 4.87 \pm 0.02$ Mpc, respectively.

We show the two projected proper length probability density functions (PDFs) in Fig. A.1. The probability that Alcyoneus has the largest projected proper length is 99.9%.[14]

Appendix B: Inclination angle comparison

In this appendix, we determine under what conditions Alcyoneus is not only the longest GRG in the plane of the sky but also in three dimensions. To this end, we compared Alcyoneus to the five previously known GRGs with projected proper lengths above 4 Mpc, which we dub 'challengers'. A challenger surpasses Alcyoneus in true proper length when

$$l_c > l, \quad \text{or} \quad \frac{l_{p,c}}{\sin\theta_c} > \frac{l_p}{\sin\theta}, \quad \text{or} \quad \sin\theta_c < \frac{l_{p,c}}{l_p}\sin\theta, \tag{B.1}$$

where l_c, $l_{p,c}$ and θ_c are the challenger's true proper length, projected proper length and inclination angle, respectively. Because the arcsine is a monotonically increasing function, a challenger surpasses Alcyoneus if its inclination angle obeys

$$\theta_c < \theta_{max,c}(\theta), \text{ where } \theta_{max,c}(\theta) := \arcsin\left(\frac{l_{p,c}}{l_p}\sin\theta\right). \tag{B.2}$$

In Fig. A.2 we show $\theta_{max,c}(\theta)$ for the five challengers with $l_{p,c} \in \{4.11\text{ Mpc}, 4.35\text{ Mpc}, 4.60\text{ Mpc}, 4.72\text{ Mpc}, 4.87\text{ Mpc}\}$ (coloured curves). Alcyoneus is least likely to be the longest GRG in 3D when its true proper length equals its projected proper length (i.e. when $\theta = 90°$). The challengers then surpass Alcyoneus in true proper length when their inclination angles are less than 55°, 61°, 67°, 71°, and 77°, respectively. For $\theta < 90°$, the conditions are more stringent.

[14] This result is insensitive to plausible changes in cosmological parameters; for example, the high-H_0 (i.e. $H_0 > 70$ km s^{-1} Mpc^{-1}) cosmology with $\mathfrak{M} = (h = 0.7020, \Omega_{BM,0} = 0.0455, \Omega_{M,0} = 0.2720, \Omega_{\Lambda,0} = 0.7280)$ yields a probability of 99.8%.

The third and fourth longest challengers, whose respective SDSS DR12 host names are J100601.73+345410.5 and J093139.03+320400.1, harbour quasars in their host galaxies. If small inclination angles distinguish quasars from non-quasar AGN, as proposed by the unification model (e.g. Hardcastle & Croston 2020), these two challengers may well be the longest radio galaxies in three dimensions.

Appendix C: Lobe volumes with truncated double cone model

C.1. Synopsis

We built an MH MCMC model, similar in spirit to the model of Boxelaar et al. (2021) for galaxy cluster halos, in order to formalise the determination of RG lobe volumes from a radio image. To this end, we introduced a parametrisation of a pair of 3D RG lobes, and explored the corresponding parameter space via the Metropolis algorithm.[15] For each parameter tuple encountered during exploration, we first calculated the MEC function of the lobes on a uniform 3D grid representing a proper (rather than co-moving) cubical volume. The RG is assumed to be far enough from the observer that the conversion to a 2D image through ray tracing simplifies to summing up the cube's voxels along one dimension, and applying a cosmological attenuation factor. This factor depends on the galaxy's cosmological redshift, which is a hyper-parameter. We blurred the model image to the resolution of the observed image, which is also a hyper-parameter. Next, we calculated the likelihood that the observed image is a noisy version of the proposed model image. We assumed thermal noise to be the dominant type of noise. If one divides the imaged sky region into patches with a solid angle equal to that of the point spread function (PSF), then the noise per patch is approximately an independent Gaussian RV. These RVs have zero mean and share the same variance, which is another hyper-parameter — typically obtained from the observed image. We chose a uniform prior over the full physically realisable part of parameter space. The resulting posterior, which contains both geometric and radiative parameters, allows one to calculate probability distributions for many interesting quantities, such as the RG's lobe volumes and inclination angle. The inferences depend weakly on cosmological parameters $\mathfrak{M}$. Furthermore, their reliability depends significantly on the validity of the model assumptions.

C.2. Model

C.2.1. Geometry

We modelled each lobe in 3D with a truncated right circular cone with apex $O \in \mathbb{R}^3$, central axis unit vector $\hat{a} \in \mathbb{S}^2$, and opening angle $\gamma \in [0, \frac{\pi}{2}]$, as in Fig. 9. The lobes share the same O, which is the RG host location. Each central axis unit vector can be parametrised through a position angle $\varphi \in [0, 2\pi)$ and an inclination angle $\theta \in [0, \pi]$. Each cone is truncated twice, through planes that intersect the cone perpendicularly to its central axis. Thus, each truncation is parametrised by the distance from the apex to the point where the plane intersects the central axis. The two inner ($d_{\mathrm{i},1}, d_{\mathrm{i},2} \in \mathbb{R}_{\geq 0}$) and two outer ($d_{\mathrm{o},1}, d_{\mathrm{o},2} \in \mathbb{R}_{\geq 0}$) truncation distances are parameters that we allowed to vary independently, with the only constraint that each inner truncation distance could not exceed the corresponding outer truncation distance.

C.2.2. Radiative processes

The radiative formulation of our model is among the simplest possible. The radio emission from the lobes is synchrotron radiation. We approximated the lobes to be perfectly optically thin and so neglected synchrotron self-absorption. The proper MEC is assumed spatially constant throughout a lobe, though possibly different among lobes; this leads to parameters $j_{\nu,1}, j_{\nu,2} \in \mathbb{R}_{\geq 0}$. The relationship between the specific intensity I_ν (in direction $\hat{r}$ at central frequency ν_c) and the MEC j_ν (in direction $\hat{r}$ at cosmological redshift z and rest-frame frequency $\nu = \nu_\mathrm{c}\,(1+z)$) is

$$I_\nu(\hat{r}, \nu_\mathrm{c}) = \int_0^\infty \frac{j_\nu(\hat{r}, z(l), \nu_\mathrm{c}(1+z(l)))}{(1+z(l))^3}\,\mathrm{d}l \approx \frac{j_\nu(\nu)\,\Delta l(\hat{r})}{(1+z)^3}, \quad \text{(C.1)}$$

where l represents proper length. The approximation is valid for a lobe with a spatially constant MEC that is small enough to assume a constant redshift for it. $\Delta l(\hat{r})$ is the proper length of the line of sight through the lobe in direction $\hat{r}$. The inferred MECs $j_{\nu,1}(\nu)$ and $j_{\nu,2}(\nu)$ thus correspond to the rest-frame frequency.

C.3. Proposal distribution

In order to explore the posterior distribution on the parameter space, we followed the Metropolis algorithm. The Metropolis algorithm assumes a symmetric proposal distribution.

C.3.1. Radio galaxy axis direction

To propose a new RG axis direction given the current one whilst satisfying the symmetry assumption, we performed a trick. We populated the unit sphere with $N \in \mathbb{N}_{\geq 1}$ points (interpreted as directions) drawn from a uniform distribution. Of these N directions, the proposed axis direction was taken to be the one closest to the current axis direction (in the great-circle distance sense). We note that this approach evidently satisfies the criterion that proposing the new direction given the old one is equally likely as proposing the old direction given the new one. We also note that the distribution of the angular distance between current and proposed axis directions is determined solely by N.

In the following paragraphs, we first review how to perform uniform sampling of the unit two-sphere. More explicitly than in Scott & Tout (1989), we then derive the distribution of the angular distance between a reference point and the nearest of N uniformly drawn other points. The result is a continuous univariate distribution with a single parameter N and finite support $(0, \pi)$. Finally, we present the mode, median and maximum likelihood estimator of N. As far as we know, these properties are new to the literature.

Uniform sampling of $\mathbb{S}^2$ Let us place a number of points uniformly on the celestial sphere $\mathbb{S}^2$. The spherical coordinates of such points are given by the RVs (Φ, Θ), where Φ denotes position angle and Θ denotes inclination angle. As all position angles are equally likely, the distribution of Φ is uniform: $\Phi \sim \mathbb{U}[0, 2\pi)$. In order to affect a uniform number density, the probability that a point lies within a rectangle of width $\mathrm{d}\varphi$ and height $\mathrm{d}\theta$ in the (φ, θ) plane equals the ratio of the solid angle of the correspond-

[15] The more general MH variant need not be considered, as we work with a symmetric proposal distribution.

ing sky patch and the sphere's total solid angle:

$$\mathbb{P}(\varphi \leq \Phi < \varphi + \mathrm{d}\varphi, \theta \leq \Theta < \theta + \mathrm{d}\theta) = \frac{\sin\theta \, \mathrm{d}\varphi \, \mathrm{d}\theta}{4\pi}. \tag{C.2}$$

The probability that the inclination angle is found somewhere in the interval $[\theta, \theta + \mathrm{d}\theta)$, regardless of the position angle, is therefore

$$\begin{aligned}\mathbb{P}(\theta \leq \Theta < \theta + \mathrm{d}\theta) &= \mathrm{d}F_\Theta(\theta) = f_\Theta(\theta)\mathrm{d}\theta \\ &= \int_0^{2\pi} \frac{\sin\theta \, \mathrm{d}\theta}{4\pi}\mathrm{d}\varphi = \frac{1}{2}\sin\theta \, \mathrm{d}\theta,\end{aligned} \tag{C.3}$$

where F_Θ is the cumulative distribution function (CDF) of Θ, and f_Θ the associated PDF. So,

$$f_\Theta(\theta) = \frac{1}{2}\sin\theta; \quad F_\Theta(\theta) := \int_0^\theta f_\Theta(\theta') \, \mathrm{d}\theta' = \frac{1 - \cos\theta}{2}. \tag{C.4}$$

Nearest-neighbour angular distance distribution Let us pick a reference point and stochastically introduce N other points in above fashion, which we dub its 'neighbours'. We now derive the PDF of the angular distance to the nearest neighbour (NNAD). Let $(\varphi_{\mathrm{ref}}, \theta_{\mathrm{ref}})$ be the coordinates of the reference point and let (φ, θ) be the coordinates of one of the neighbours. Without loss of generality, due to spherical symmetry, we can choose to place the reference point in the direction towards the observer: $\theta_{\mathrm{ref}} = 0$. (We note that φ_{ref} is meaningless in this case.) The angular distance between two points on $\mathbb{S}^2$ is given by the great-circle distance ξ. For our choice of reference point, we immediately see that $\xi(\varphi_{\mathrm{ref}}, \theta_{\mathrm{ref}}, \varphi, \theta) = \theta$.

Because θ is a realisation of Θ, ξ too can be regarded as a realisation of an RV, which we call Ξ. Evidently, the PDF $f_\Xi(\xi) = f_\Theta(\xi)$ and the CDF $F_\Xi(\xi) = F_\Theta(\xi)$.

Now we consider the generation of N points, whose angular distances to the reference point are the RVs $\{\Xi_i\} := \{\Xi_1, ..., \Xi_N\}$. The NNAD RV M is the minimum of this set: $M := \min\{\Xi_i\}$. We next determine the CDF F_M and PDF f_M of M by noting that

$$\begin{aligned}F_M(\mu) := \mathbb{P}(M \leq \mu) &= \mathbb{P}(\text{minimum of } \{\Xi_i\} \leq \mu) \\ &= \mathbb{P}(\text{at least one of the set } \{\Xi_i\} \leq \mu) \\ &= 1 - \mathbb{P}(\text{none of the set } \{\Xi_i\} \leq \mu) \\ &= 1 - \mathbb{P}(\text{all of the set } \{\Xi_i\} > \mu).\end{aligned} \tag{C.5}$$

Because the $\{\Xi_i\}$ are independent and identically distributed,

$$\begin{aligned}F_M(\mu) &= 1 - \prod_{i=1}^N \mathbb{P}(\Xi_i > \mu) \\ &= 1 - \mathbb{P}^N(\Xi > \mu) = 1 - (1 - F_\Xi(\mu))^N.\end{aligned} \tag{C.6}$$

By substitution, the application of a trigonometric identity and differentiation to μ, we obtain the CDF and PDF of M:

$$F_M(\mu) = 1 - \cos^{2N}\left(\frac{\mu}{2}\right); \; f_M(\mu) = N\sin\left(\frac{\mu}{2}\right)\cos^{2N-1}\left(\frac{\mu}{2}\right). \tag{C.7}$$

In Fig. C.1, we show this PDF for various values of N.
The mode of M (i.e. the most probable NNAD), μ_{mode}, is the solution to $\frac{\mathrm{d}f_M}{\mathrm{d}\mu}(\mu_{\mathrm{mode}}) = 0$. The median of M, μ_{median}, is the solution to $F_M(\mu_{\mathrm{median}}) = \frac{1}{2}$. Hence,

$$\mu_{\mathrm{mode}} = \arccos\left(1 - \frac{1}{N}\right); \; \mu_{\mathrm{median}} = \arccos\left(2^{1-\frac{1}{N}} - 1\right). \tag{C.8}$$

As common sense dictates, both equal $\frac{\pi}{2}$ for $N = 1$ and tend to 0 as $N \to \infty$. We find the mean of M through integration by parts:

$$\begin{aligned}\mathbb{E}[M] &:= \int_0^\pi \mu f_M(\mu) \, \mathrm{d}\mu = \int_0^\pi \mu \, \mathrm{d}F_M(\mu) \\ &= \left[\mu F_M(\mu)\right]_0^\pi - \int_0^\pi F_M(\mu) \, \mathrm{d}\mu \\ &= \int_0^\pi \cos^{2N}\left(\frac{\mu}{2}\right)\mathrm{d}\mu = 2\int_0^{\frac{\pi}{2}} \cos^{2N}(\mu) \, \mathrm{d}\mu.\end{aligned} \tag{C.9}$$

Again via integration by parts,

$$\mathbb{E}[M] = \pi\prod_{k=1}^N \frac{2k-1}{2k} = \frac{\pi}{2^{2N}}\binom{2N}{N}. \tag{C.10}$$

Maximum likelihood estimation A typical application is the estimation of N in the PDF $f_M(\mu \mid N)$ (Eq. C.7) using data. We assume we have measured k NNADs, denoted by $\{\mu_1, ..., \mu_k\}$. Let the joint PDF or likelihood be

$$\begin{aligned}\mathcal{L}(N) &:= \prod_{i=1}^k f_M(\mu_i \mid N) \\ &= \left(\frac{N}{2^N}\right)^k \prod_{i=1}^k \sin\mu_i \, (\cos\mu_i + 1)^{N-1}.\end{aligned} \tag{C.11}$$

To find N_{MLE}, we look for the value of N that maximises $\mathcal{L}(N)$. To simplify the algebra, we could however equally well maximise a k-th of the natural logarithm of the likelihood, or the average log-likelihood $\hat{l} := k^{-1}\ln\mathcal{L}(N)$, because the logarithm is a monotonically increasing function:

$$\begin{aligned}\hat{l}(N) &:= \frac{1}{k}\ln\mathcal{L}(N) = \ln N - N\ln 2 \\ &+ \frac{1}{k}\sum_{i=1}^k \ln\sin\mu_i + (N-1)\ln(\cos\mu_i + 1).\end{aligned} \tag{C.12}$$

We find N_{MLE} by solving $\frac{\mathrm{d}\hat{l}}{\mathrm{d}N}(N_{\mathrm{MLE}}) = 0$. This leads to

$$N_{\mathrm{MLE}} = \left(\ln 2 - \frac{1}{k}\sum_{i=1}^k \ln(\cos\mu_i + 1)\right)^{-1}. \tag{C.13}$$

An easy limit to evaluate is the case when $\mu_1, ..., \mu_k \to 0$. In such a case, $\cos\mu_i \to 1$, and so $\frac{1}{k}\sum_{i=1}^k \ln(\cos\mu_i + 1) \to \ln 2$. Then, $N_{\mathrm{MLE}} \to (0_+)^{-1} \to \infty$. This is expected behaviour: when all measured NNADs approach 0, the number of points distributed on the sphere must be approaching infinity.

C.3.2. Other parameters

The other proposal parameters were each drawn from independent normal distributions centred around the current parameter values. These proposal distributions are evidently symmetric but have support over the full real line, so forbidden parameter values could in principle be proposed. As a remedy, we set the prior probability density of the proposed parameter set to 0 when the proposed opening angle was negative or exceeded $\frac{\pi}{2}$ rad, at least one of the proposed MECs was negative, or when at least one of the proposed inner truncation distances was negative or exceeded the corresponding proposed outer truncation

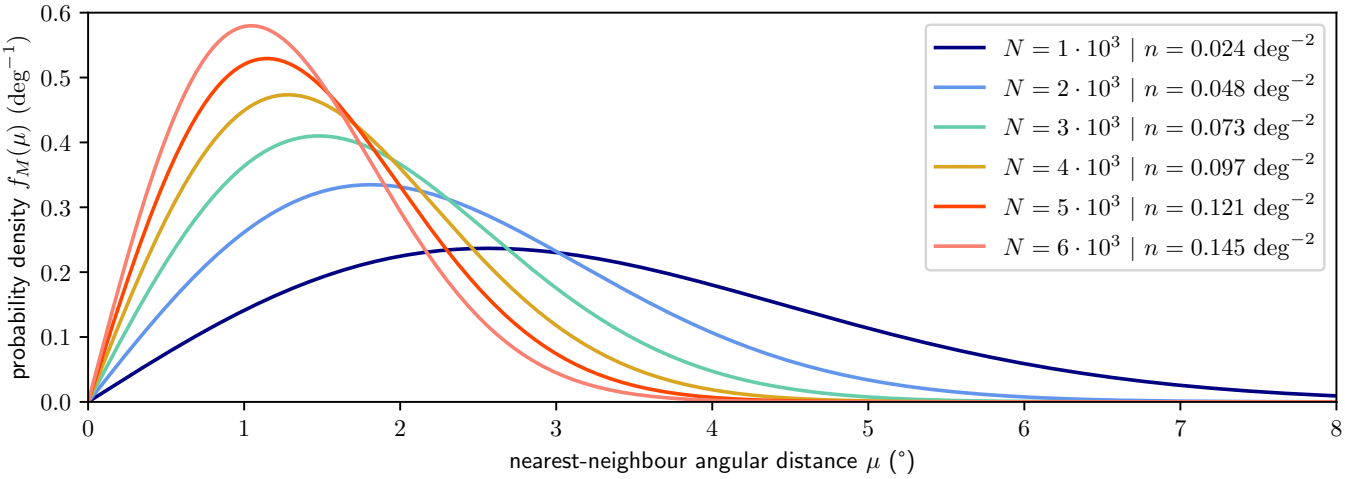

Fig. C.1. PDFs of the NNAD RV M between some fixed point and N other points distributed randomly over the celestial sphere. As the sphere gets more densely packed, the probability of finding a small M increases. For each N, we provide the equivalent mean point number density, n.

distance. In such cases, the posterior probability density was 0 too, as it is proportional to the prior probability density. Consequently, the Metropolis acceptance probability vanished and the proposal was rejected. We did not enter forbidden regions of parameter space. The condition of detailed balance was still respected: probability densities for transitioning *towards* the forbidden region were 0, just as probability densities for being in the forbidden region.

C.4. Likelihood

Assuming thermal noise to be the dominant noise type, we took the likelihood to be Gaussian. To avoid dimensionality errors, we multiplied the likelihood by a constant before we applied the logarithm:

$$\ln\left(\mathcal{L}\cdot\left(\sigma\sqrt{2\pi}\right)^{N_\mathrm{r}}\right) = -\frac{N_\mathrm{r}}{2\sigma^2 N_\mathrm{p}}\sum_{i=1}^{N_\mathrm{p}}\left(I_{\nu,\mathrm{o}}[i]-I_{\nu,\mathrm{m}}[i]\right)^2. \tag{C.14}$$

Here, σ is the image noise, $N_\mathrm{r}\in\mathbb{R}_{\geq 0}$ is the number of resolution elements (i.e. PSF solid angles) in the image, $N_\mathrm{p}\in\mathbb{N}$ is the number of pixels in the image, and $I_{\nu,\mathrm{o}}[i]$ and $I_{\nu,\mathrm{m}}[i]$ are the i-th pixel values of the observed and modelled image, respectively. For simplicity, one may multiply the likelihood by a constant factor (or, equivalently, add a constant term to the log-likelihood): the acceptance ratio will remain the same, and the MH MCMC runs correctly.

C.5. Results for Alcyoneus

We applied the Bayesian model to the 90″ LoTSS DR2 image of Alcyoneus, shown in the top panel of Fig. 9. Thus, the hyperparameters were $z = 0.24674$, $\nu_\mathrm{c} = 144$ MHz (so that $\nu = 180$ MHz), $\theta_\mathrm{FWHM} = 90''$, $N = 750$ and $\sigma = \sqrt{2}\cdot 1.16$ Jy deg^{-2}. We set the image noise to $\sqrt{2}$ times the *true* image noise to account for model incompleteness. This factor follows by assuming that the inability of the model to produce the true lobe morphology yields (Gaussian) errors comparable to the image noise. To speed up inference, we down-sampled the image of 2,048 by 2,048 pixels by a factor of 16 along each dimension. We ran our MH MCMC for 10,000 steps and discarded the first 1,500 steps due to burn-in.

Table C.1. Maximum a posteriori probability (MAP) estimates and posterior mean and standard deviation (SD) of the parameters from the Bayesian, doubly truncated, conical RG lobe model of Sect. 3.9.

parameter	MAP estimate	posterior mean and SD
φ_1	307°	307 ± 1°
φ_2	140°	139 ± 2°
$\lvert\theta_1 - 90°\rvert$	54°	51 ± 2°
$\lvert\theta_2 - 90°\rvert$	25°	18 ± 7°
γ_1	9°	10 ± 1°
γ_2	24°	26 ± 2°
$d_{\mathrm{i},1}$	2.7 Mpc	2.6 ± 0.2 Mpc
$d_{\mathrm{o},1}$	4.3 Mpc	4.0 ± 0.2 Mpc
$d_{\mathrm{i},2}$	1.6 Mpc	1.5 ± 0.1 Mpc
$d_{\mathrm{o},2}$	2.0 Mpc	2.0 ± 0.1 Mpc
$j_{\nu,1}(\nu)$	17 Jy deg^{-2} Mpc^{-1}	17 ± 2 Jy deg^{-2} Mpc^{-1}
$j_{\nu,2}(\nu)$	22 Jy deg^{-2} Mpc^{-1}	18 ± 3 Jy deg^{-2} Mpc^{-1}

Table C.1 lists the obtained maximum a posteriori probability estimates and posterior mean and standard deviation of the parameters.

The proper volumes V_1 and V_2 are derived quantities:

$$V = \frac{\pi}{3}\tan^2\gamma\left(d_\mathrm{o}^3 - d_\mathrm{i}^3\right), \tag{C.15}$$

just like the flux densities $F_{\nu,1}(\nu_\mathrm{c})$ and $F_{\nu,2}(\nu_\mathrm{c})$ at central frequency ν_c:

$$F_\nu(\nu_\mathrm{c}) = \frac{j_\nu(\nu)\,V}{(1+z)^3\,r_\phi^2(z)}. \tag{C.16}$$

Together, V and $F_\nu(\nu_\mathrm{c})$ imply a lobe pressure P and a magnetic field strength B, which are additional derived quantities that we calculate through `pysynch`. Table C.2 lists the obtained MAP estimates and posterior mean and standard deviation of the derived quantities.

The uncertainties of the parameters and derived quantities reported in Tables C.1 and C.2 are not necessarily independent. To demonstrate this, we present MECs and volumes from the MH MCMC samples in Fig. C.2. MECs and volumes do not vary independently, because their product is proportional to flux

Table C.2. Maximum a posteriori probability (MAP) estimates and posterior mean and standard deviation (SD) of derived quantities from the Bayesian, doubly truncated, conical RG lobe model of Sect. 3.9.

derived quantity	MAP estimate	posterior mean and SD
$\Delta\varphi$	167°	168 ± 2°
V_1	1.5 Mpc^3	1.5 ± 0.2 Mpc^3
V_2	0.8 Mpc^3	1.0 ± 0.2 Mpc^3
$F_{\nu,1}(\nu_c)$	63 mJy	63 ± 4 mJy
$F_{\nu,2}(\nu_c)$	44 mJy	45 ± 5 mJy
$P_{\mathrm{min},1}$	4.7×10^{-16} Pa	$4.8 \pm 0.3 \times 10^{-16}$ Pa
$P_{\mathrm{min},2}$	5.4×10^{-16} Pa	$5.0 \pm 0.6 \times 10^{-16}$ Pa
$P_{\mathrm{eq},1}$	4.8×10^{-16} Pa	$4.9 \pm 0.3 \times 10^{-16}$ Pa
$P_{\mathrm{eq},2}$	5.4×10^{-16} Pa	$5.0 \pm 0.6 \times 10^{-16}$ Pa
$B_{\mathrm{min},1}$	45 pT	45 ± 1 pT
$B_{\mathrm{min},2}$	48 pT	46 ± 3 pT
$B_{\mathrm{eq},1}$	42 pT	43 ± 1 pT
$B_{\mathrm{eq},2}$	45 pT	43 ± 3 pT
$E_{\mathrm{min},1}$	6.3×10^{52} J	$6.2 \pm 0.4 \times 10^{52}$ J
$E_{\mathrm{min},2}$	3.7×10^{52} J	$4.4 \pm 0.6 \times 10^{52}$ J
$E_{\mathrm{eq},1}$	6.4×10^{52} J	$6.3 \pm 0.4 \times 10^{52}$ J
$E_{\mathrm{eq},2}$	3.8×10^{52} J	$4.4 \pm 0.6 \times 10^{52}$ J

density (see Eq. C.16); only realistic flux densities correspond to high-likelihood model images.

Finally, we explored a simpler variation of the model, in which we forced the lobes to be coaxial. In such a case, the

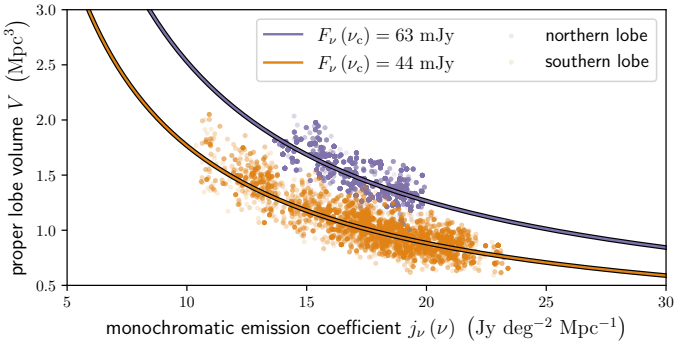

Fig. C.2. Strongly correlated estimates of $j_\nu(\nu)$ and V from our Bayesian model, demonstrating consistency with the observed lobe flux densities. We show MECs $j_\nu(\nu)$ at $\nu = 180$ MHz and proper volumes V of MH MCMC samples for the northern lobe (purple dots) and southern lobe (orange dots). The curves represent all combinations $(j_\nu(\nu), V)$ that correspond to a particular flux density at the LoTSS central wavelength $\nu_c = 144$ MHz. We show the observed northern lobe flux density (purple curve) and the observed southern lobe flux density (orange curve).

true proper length l and projected proper length l_p are additional derived quantities:

$$l = \frac{d_{o,1} + d_{o,2}}{\cos\gamma}; \quad l_p = l \sin\theta. \tag{C.17}$$

For Alcyoneus, this simpler model does not provide a good fit to the data.